On the Robustness of the Interdecadal Modes of the Thermohaline Circulation

THIERRY HUCK AND GEOFFREY K. VALLIS

Princeton University AOS/GFDL, Princeton, New Jersey

ALAIN COLIN DE VERDIÈRE

Laboratoire de Physique des Océans, Université de Bretagne Occidentale, Brest, France

(Manuscript received 9 June 1999, in final form 22 February 2000)

ABSTRACT

Ocean models in box geometry forced by constant surface fluxes of density have been found to spontaneously generate interdecadal oscillations of the thermohaline circulation. This paper analyzes the sensitivity of these oscillations to various physical effects, including the presence of mesoscale turbulence, various thermal surface boundary conditions, and the presence of wind forcing or bottom topography. The role of unstable long baroclinic waves is also reexamined in an attempt to understand the oscillation period.

In idealized geometry, it is found that the low-frequency variability of the thermohaline circulation under quasi-constant surface fluxes is a robust feature of the large-scale circulation. It is not strongly affected by energetic mesoscale turbulence; the oscillation period is relatively invariant with respect to varying resolution and momentum and tracer horizontal mixing coefficients, although it loses some regularity as shorter and longer periods of variability emerge when the mesoscale activity increases in strength with smaller mixing coefficients. The oscillations are also retained as the ocean model is coupled to an interactive atmospheric energy balance model; the thermohaline modes are robust to a range of exchange coefficients that widens with the amplitude of the mean circulation. The presence of an additional wind-forced component generally weakens the oscillation, and depending on the relative strength of thermodynamic and dynamic forcings, the oscillation may be completely killed. A simple interpretation is given, highlighting the role of upward Ekman pumping in damping density anomalies. Finally, the interaction of these baroclinic modes with bottom topography depends strongly on the relative directions of the mean topographic features and the mean currents and baroclinic waves, but usually results in a damping influence.

1. Introduction

Natural variability of the climate system is undoubtedly responsible for part of the long-term climate changes that have been observed during the last decades, for instance in the North Atlantic. Analysis of the observations of the last century sea surface and atmospheric data in the North Atlantic have shown interdecadal oscillations (Bjerknes 1964; Kushnir 1994), confirmed by reconstructed time series on multiple centuries (Mann et al. 1998; Delworth and Mann 2000). Numerical coupled models have succeeded in producing interdecadal modes of variability in the North Atlantic. Delworth et al. (1993) described a 50-yr oscillation in the Geophysical Fluid Dynamics Laboratory (GFDL) coupled model related to changes in the thermohaline circulation through advection of density anomalies in the convection regions; Timmermann et al. (1998) discussed oscillations of about 35 yr in the Max Planck Institute coupled model actively involving the North Atlantic Oscillation. Ocean models spontaneously generate somewhat similar oscillations under constant heat and freshwater forcing (Greatbatch and Zhang 1995); in fact, the heat flux is sufficient to drive the variability, while the active salinity reduces the amplitude of the oscillations. It appears also in observations that temperature anomalies in the North Atlantic are often associated with salinity anomalies of the same sign, but the temperature influence on density prevails (e.g., McCartney et al. 1996). Nevertheless, Delworth and Greatbatch (2000) recently found that the interdecadal mode in the GFDL coupled model is not sustained in the ''ocean only'' model forced with the seasonally varying ''climatological'' surface fluxes, but reappears with somewhat reduced amplitude when random time series of the coupled simulation heat fluxes are used, in agreement with the interpretation of these oscillations as a damped thermohaline oscillator excited by stochastic atmospheric forcing (Griffies and Tziperman 1995).

Corresponding author address: Thierry Huck, Laboratoire de Physique des Océans, Université de Bretagne Occidentale, UFR Sciences F308, 6 avenue Le Gorgeu, B.P. 809, 29285 Brest Cedex, France.
E-mail: thuck@univ-brest.fr

Ultimately, the thermohaline oscillation seems to arise because of a delay between the transport of heat by the mean meridional circulation and the meridional temperature gradient, but the problem is in the details in understanding what produces the period, amplitude, and energy source of these oscillations. That is to say, the mechanism of the oscillation is, unfortunately, not completely understood, and thus its sensitivity to poorly determined physical parameters in the ocean (e.g., the vertical and horizontal mixing coefficient) is not well known. For example, a number of recent studies have noted the sensitivity of this interdecadal mode of the thermohaline circulation to various subgridscale parameters (Huck et al. 1999a, HCW hereafter), to bottom topography (Winton 1996; Greatbatch et al. 1997) and to forcing (Chen and Ghil 1996), but without suggesting any particular mechanism or reason for the sensitivity.

Regarding the mechanisms of the oscillator, Winton (1996) and Greatbatch and Peterson (1996) had suggested that frictional boundary waves (the analog of Kelvin waves in planetary geostrophic ocean models) might provide the right timescales when they are slowed down in very weakly stratified regions (like convection regions along the poleward boundary). However, HCW found that the propagation of such waves was not, in fact, necessary to sustain the oscillations. Baroclinic Rossby waves based on the β effect had also seemed a most likely candidate to produce interdecadal timescales, until Winton (1996) was able to reproduce oscillations of the same character on f planes. HCW and Colin de Verdière and Huck (1999, CVH hereafter) suggested that more general ''potential vorticity waves,'' analogous to Rossby waves but relying on the mean stratification rather than the β effect, might be the ''adjustment waves'' whose propagation across the basin sets up the regular oscillations period. CVH also suggested that long-wave baroclinic instability of the western boundary current (where it separates from the coast) is the ''wavemaker'' (i.e., the energy source) for interdecadal oscillations. The typical growth rate they calculated from linear stability analysis of the vertical profiles of velocities and densities in the most unstable regions, as well as diagnostics from the variance terms in the models, were rather small, of the order of one cycle per year. This value seemed to agree well with the critical damping terms—the horizontal diffusion of tracer and coupling with the atmosphere, of the order of 2500 $m^2\ s^{-1}$ and 22 $W\ m^{-2}\ K^{-1}$, respectively (HCW). The similarity of these values to the ones commonly used in ocean models may justify the different results found in the literature about models oscillating or not.

The effects of surface boundary conditions on such oscillations was examined by HCW, Fanning and Weaver (1996), and Chen and Ghil (1995). HCW found that the oscillations were quite sensitive to the Haney-like exchange coefficient of sensible heat between ocean and fixed atmosphere within restoring boundary conditions: if this value went above about 22 $W\ m^{-2}\ K^{-1}$ oscillations were no longer produced. Chen and Ghil (1996) subsequently reproduced similar decadal oscillations when they coupled their ocean model to a very simple energy balance atmosphere model, also finding a sensitivity to the analogous heat-exchange coefficient. It remains unclear, however, whether the oscillations will persist with a more complex atmospheric model. Along similar lines, oscillations of the thermohaline circulation appear sensitive to the vertical mixing. For example, HCW found oscillations only if the vertical mixing was larger than about $0.2 \times 10^{-4}\ m^2\ s^{-1}$, which is close to many current estimates at least in the open ocean away from topography (e.g., Ledwell et al. 1993)—but because of idealized configuration and surface boundary conditions their thermohaline circulation was extremely weak with reduced mixing.

Regarding the lower boundary conditions, Winton (1997) and Greatbatch et al. (1997) stressed the damping influence of variable bottom topography on these baroclinic modes. The recent understanding of the driving mechanism for the oscillations as well as the suggested setting of the period by potential vorticity waves on the mean circulation and stratification (instead of the previously supposed viscous boundary ''Kelvin'' waves) might restrict the expected influence of the bottom topography around some critical damping parameters, and too few experiments have been done so far to establish with no doubt the nonexistence of these interdecadal modes within variable bottom topography.

Finally, the sensitivity of the oscillations to changing model resolution, and in particular the presence of mesoscale eddies, has not been extensively studied, save for some weakly turbulent eddy-permitting simulations by Fanning and Weaver (1998) still showing sensitivity to subgridscale parameterizations.

Thus, although there have been quite a large number of studies, the results have been equivocal as what determines the amplitude and temporal scale of the oscillations, and what parameters they are most sensitive too. The problem in interpreting all of the various results arises in part because many different models and boundary conditions have been used, making direct comparisons all but impossible. The purpose of this paper is to investigate the above issues in a systematic, step-by-step way, and the paper itself is organized similarly. The basic oscillation mechanism is reviewed in section 2. We follow this by a sequential analysis of the sensitivity of the interdecadal modes of the thermohaline circulation to mesoscale turbulence (section 3), coupling with a simplified atmosphere (section 4), the interaction with the wind forcing (section 5) and bottom topography (section 6). Section 7 concludes our analysis.

2. The basic mechanism

The simplest configuration of a three-dimensional, dynamical, ocean model that sustains interdecadal oscillations is a midlatitude flat-bottom basin forced by

constant zonally uniform surface fluxes of density, through either freshwater (Huang and Chou 1994) or heat (Greatbatch and Zhang 1995). This section describes the generic configuration we use throughout the paper, the basic oscillation and its mechanism, and a scale analysis for the oscillation period.

a. A simple configuration

To illustrate the basic mechanism, we use a planetary geostrophic model with Laplacian viscosity in Cartesian geometry (see Huck et al. 1999b, HWC hereafter). The model is configured in flat-bottomed β-plane basin centered at 40°N and extending from 20° to 60°N, 60° wide, 4500 m deep. Density is dependent only on temperature, through a linear equation of state: $\rho = \rho_0(1 - \alpha T)$, $\alpha = 2 \times 10^{-4}$ K^{-1}. The surface forcing consists of fixed zonally uniform heat fluxes varying linearly with latitude from 45 W m^{-2} at 20°N to -45 W m^{-2} at 60°N and zero wind stress. The horizontal resolution is 160 km (experiment referenced as ''L160'' hereafter), while the vertical discretization has 15 levels, varying in thickness from 50 m at the surface to 550 m at depth. Subgridscale parameterizations are implemented as simply as possible, using spatially uniform mixing coefficients. Relatively intense vertical mixing of heat (10^{-4} m^2 s^{-1}) is necessary to drive a meridional overturning cell of reasonable amplitude O(10 Sv). Horizontal mixing of heat (700 m^2 s^{-1}) is in the range of estimates from Lagrangian float dispersion, whereas horizontal mixing of momentum (10^5 m^2 s^{-1}) ensures the resolution of the Munk western boundary layer within the actual gridspacing.

The mean circulation is then an anticyclonic subtropical gyre in the upper layers, with deep water formation in the northeast corner feeding the opposite circulation at depth (such that the barotropic flow cancels in the absence of wind forcing, bottom topography, and bottom drag). In spite of the constant forcing, the model does not settle in a steady state but rather goes on perpetual oscillations of period 25.5 yr.

b. Description of the oscillation

It is likely that the oscillations described by Greatbatch and Zhang (1995), Chen and Ghil (1995, 1996), Winton (1996), Greatbatch and Peterson (1996), HCW, and possibly others, all have the same underlying physical mechanism. Let us first recapture the oscillation in a very simple setting, with a view to understanding the basic features of the mechanism. To synthesize the broad oscillation picture, an empirical orthogonal function (EOF) analysis, or principal component analysis, is performed on the four-dimensional (space–time) temperature field for the previously described experiment, through 51 annual snapshots over two oscillation periods (2×25.5 yr). Two eigenvalues of the covariance matrix capture most of the variance, respectively, 53% and 36%. Their time series (Fig. 1) and horizontal structure in the upper 50 m (Fig. 2) show a complex evolution of the anomalies along the major current pathways and along the northern boundary. The anomalous velocities in the upper layers are in good geostrophic balance with the surface temperature anomalies due to the weakness of the anomalies at depth.

The same analysis is performed for the meridional overturning streamfunctions: a single EOF now explains most of the variance (88%) and is concentrated in the most poleward 5° of latitude, such that it induces a strong reversed thermohaline cell when its amplitude is negative. The oscillation is strongly linked to these changes in the meridional overturning and western boundary current (WBC) transport.

In order to draw a heuristic picture of the oscillation, let us start at year 4 when the temperature anomaly field is more or less the negative of EOF 2 itself (see Fig. 1a): a large positive anomaly is centered at 35°N, 9°E (on the east side of the WBC) and extends northwestward then eastward with larger amplitude along the mean current path. Note the negative anomaly along the northern boundary centered at 33°E. The overturning is close to its time average value, but with negative temperature anomalies having filled the northern regions for the previous decade, it is increasing. The temperature anomaly field subsequently evolves into an EOF 1 structure (yr 12), associated with maximum overturning, WBC transport and poleward heat transport, and with a much-reduced meridional density gradient. The negative anomaly along the northern boundary has been propagating westward by 13°, while a positive anomaly now occupies the eastern half of the northern boundary. The meridional density gradient being now reduced, the still increasing overturning is clearly unstable, and a breakdown occurs within a few years, restoring the overturning and poleward heat transport to a minimum. Simultaneously, the negative temperature anomaly along the northern boundary has reached the western boundary (and maybe helped reversing the WBC anomalous transport). The temperature field evolves rapidly into EOF 2 structure (yr 17) because of the sharp reduction in northward transport of heat. The positive anomaly along the northern boundary has started its westward propagation. Toward yr 22 (the opposite phase of EOF 1), the southern half of the basin is warming while the northern half is cooling. The meridional density gradient is building up along with the meridional overturning. A negative temperature anomaly now fills the eastern half of the northern boundary while the positive anomaly propagates westward. As the meridional cell and poleward heat transport intensify, the western boundary current path starts warming up and splits the large EOF 1 temperature lobe into the northern boundary anomaly and a residual stationary cyclonic lobe centered at 47°N, 23°E.

Essential to the oscillatory behavior is the time lag between meridional density gradient anomalies and

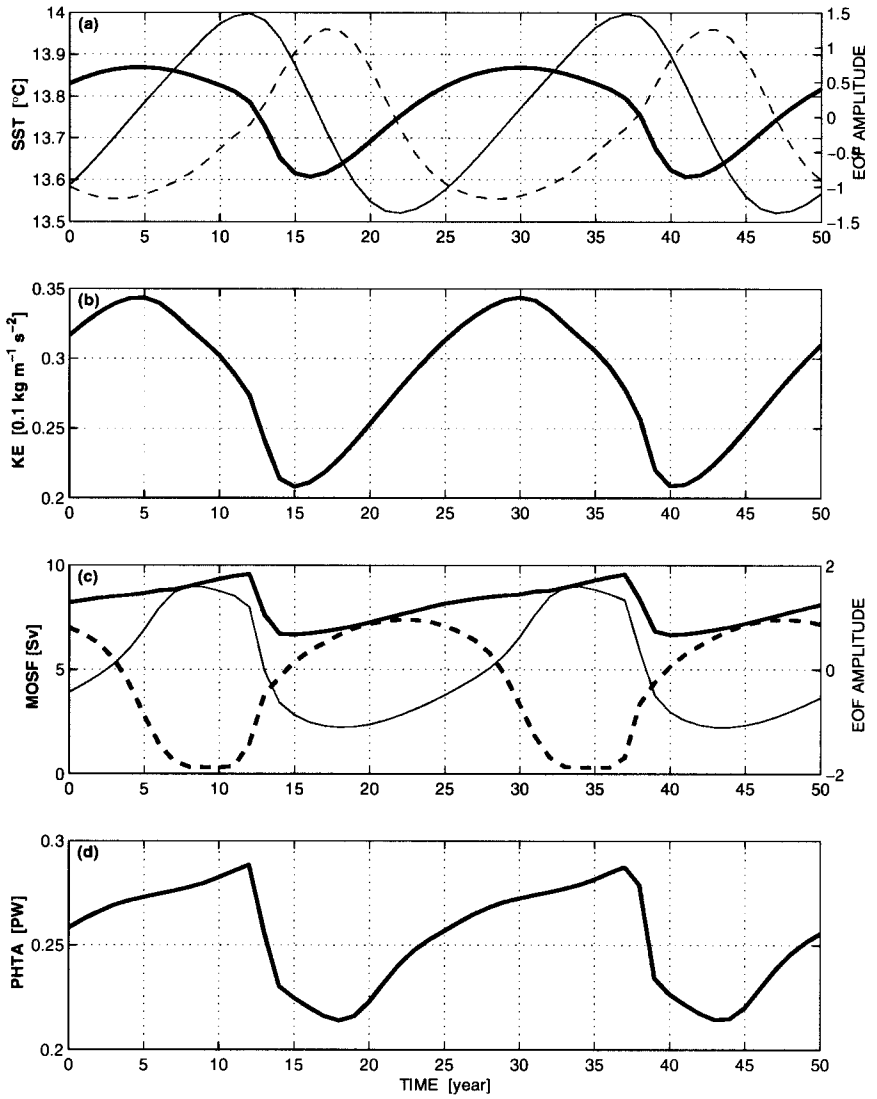

FIG. 1. Time evolution of various diagnostics in a coarse resolution experiment (L160): (a) mean surface temperature (upper 50 m, thick) and first two EOFs (thin: EOF 1 solid, EOF 2 dashed) time series; (b) total kinetic energy; (c) meridional overturning maximum (thick), minimum (dashed, as its opposite), and first EOF (thin) time series; (d) maximum advective poleward heat transport.

overturning response through baroclinic planetary waves propagation on decadal timescales (Greatbatch and Peterson 1996; HCW; Colin de Verdière and Huck 2000).

It is not clear whether the propagation of temperature anomalies westward along the northern boundary is essential to the oscillation, but it is the only sign of baroclinic adjustment we could find under zonally uniform surface fluxes. Such a propagation is not observed in the oscillations under constant fluxes diagnosed from a restoring run, as described in HCW, where the variability is restricted to the northwest corner (where the surface fluxes are intensified). In both cases, variations of temperature along the northern boundary are considerably smaller than variations in the ocean interior due to changes in the overturning circulation. Although boundary waves and baroclinic waves do undoubtedly realize the baroclinic adjustment, their thermal signature and pathway are hardly identified in the simulations: the modifications of the circulation and thus temperature they cause totally conceal their propagation. This propagation has been interpreted in terms of viscous boundary waves (Winton 1996; Greatbatch and Peterson 1996), but we propose an alternative interpretation below.

c. The baroclinic instability mechanism

From the EOF analysis, as well as from Hovmöller diagrams of temperature along the northern boundary

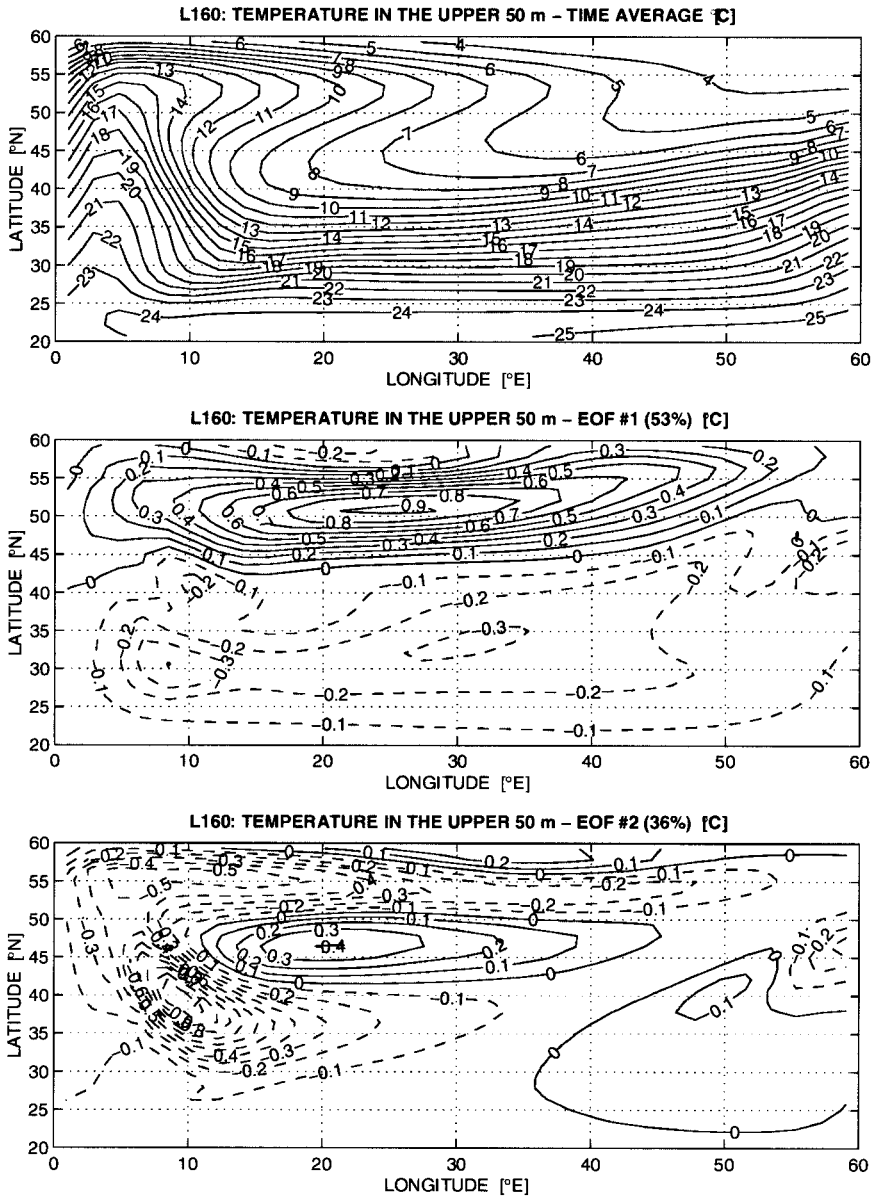

FIG. 2. Evolution of the upper 50-m temperature in a coarse resolution experiment (L160): (a) time average, (b) first, and (c) second EOF, whose time series are shown in Fig. 1. A composite analysis, differentiating the surface temperature at times with high vs low kinetic energy, shows a structure very similar to the opposite of EOF 2, with amplitude of up to 4° and −2°C.

as a function of time (not shown), we can estimate accurately the propagation speed as well as the vertical structure of the anomalies. Negative (positive) temperature anomalies take 12 (16) yr to cross the basin from east to west (5120 km) giving an average speed of 1.2 cm s^{-1}. The fronts of the anomalies have a baroclinic temperature anomaly structure while the core of the anomalies extends much deeper with no sign reversal at depth. Figure 3 shows vertical profiles of the EOFs in the core of the main lobes and along the northern boundary. The former have a baroclinic structure while the latter are of one sign on the vertical with a deeper extent of the surface intensified amplitude. As we shall see, the former (latter) resemble the second (first) baroclinic modes.

To address the vertical structure, propagation and instability of the waves on the mean stratification and circulation, local linear stability calculations are performed in the quasigeostrophic (QG hereafter) approximation, following Beckmann (1988). In a second stage, we also include the mean meridional velocities (Pedlosky 1979) with little changes in the maximum growth rate. In both cases, the actual viscosity of the three-dimensional model is used for the dissipation, which

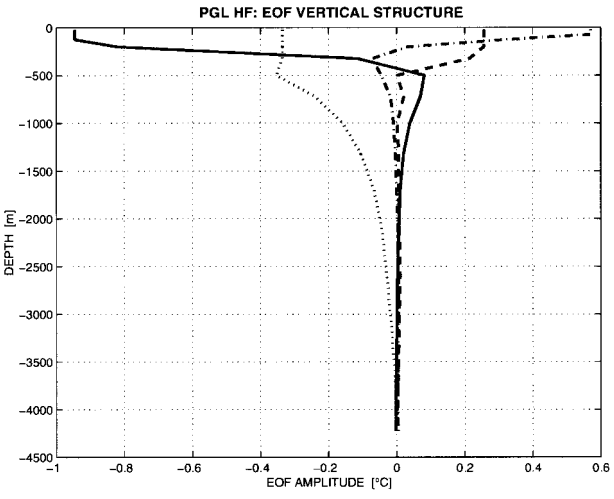

FIG. 3. Vertical structure of the temperature EOFs for the coarse-resolution simulation (L160): EOF 1 main lobe centered at 51°N, 25°E (solid) and northern lobe centered at 59°N, 20°E (dashed). EOF 2 northwest lobe centered at 55°N, 7°E (dash-dotted) and northern lobe centered at 59°N, 32°E (dotted).

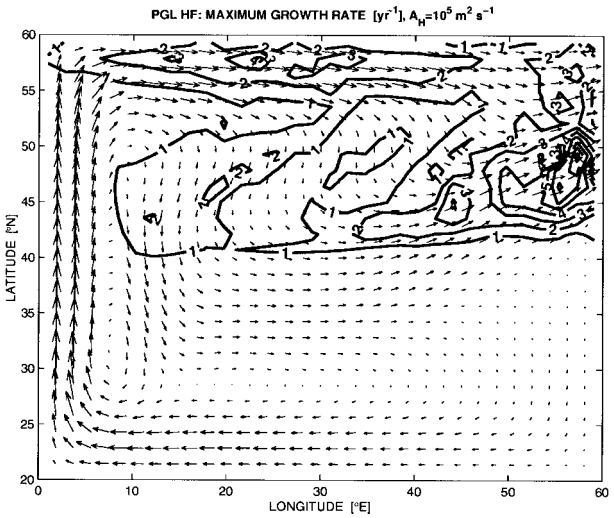

FIG. 4. Maximum growth rate of baroclinic instability (yr^{-1}) at each horizontal location for the time-averaged vertical profiles of density and velocities of the coarse-resolution model (L160) with a viscosity of 10^5 m^2 s^{-1}. The arrows are the time-averaged model velocities in the upper 250 m, the scale is 2 cm s^{-1} per degree of latitude or longitude.

strongly shifts the most unstable wave to lower wavenumbers along with reducing the maximum growth rate.

We first apply the computation to the vertical profiles of the time-averaged density and velocity for each horizontal grid point of the model, and keep the larger growth rate over wavenumber and wave direction (Fig. 4). This draws attention to three regions with local maximum of the growth rate: the northeastern region ($45°N < \theta < 50°N$, $53°E < \phi < 60°E$) with the largest growth rate overall reaching 8 yr^{-1}, the northern boundary region with growth rate reaching 4 yr^{-1}, and a region east of the western boundary current ($43°N < \theta < 49°N$, $13°E < \phi < 20°E$) hardly reaching 3 yr^{-1}. Similar calculations performed for snapshots taken every year during one oscillation period do not show significant variations in time, except for the location of the maximum values along the northern boundary. Baroclinic instability actually exists in the long-wave limit of these QG calculations, as previously shown by Colin de Verdière (1986) in the planetary geostrophic approximation.

Finally, the density and velocity profiles are averaged zonally and over the northern 640 km (as suggested by the meridional extent of the boundary waves) as well as in time, and the instability calculations are performed (Fig. 5). The most unstable wave has a growth rate of the order of 0.5 yr^{-1} and a wavelength of 250 km for the model viscosity (note the large influence of this process on the growth rate and most unstable wavenumber). Its vertical structure (shown in Fig. 5b) is more surface intensified than the stratification modes, and may be compared to the EOF vertical structure (note that the EOF structure is for temperature while the baroclinic eigenmode calculations is for the streamfunction or horizontal velocities). Finally, its westward group velocity is of the order of 2.8 cm s^{-1}, and does not depend on the β effect but solely on the meridional slope of the isopycnals providing the mean eastward current shear, as measured by $(U_z f^2/N^2)_z$.

In conclusion, these unstable baroclinic waves propagating westward and growing on the mean stratification and circulation of the northern region of the domain provide a plausible explanation for the variability: their positive growth rate might explain the sustainability of the oscillations against dissipation (horizontal diffusion mainly) whereas their propagation along the northern boundary might set the oscillation period. Although the actual westward velocity of the temperature anomalies is twice as small as the most unstable wave's speed, processes like heat diffusion and convection (as well as nonlinearities) are not considered in the QG calculation, and their influence on the thermohaline circulation is not yet clear. In contrast, CVH pointed out the instability of the western boundary current region as responsible for the variability when the surface fluxes were intensified in the northwest region.

d. The oscillation period

Although it is most likely that baroclinic instability is the source of energy for the oscillation, it might not determine its period; linear stability calculations suggest that the periods associated with the most unstable waves are too short—of order (1 month)—to be a direct cause. We thus build on the hypothesis that the oscillation period that emerges is a near-resonant or global mode of the basin, in terms of potential vorticity (PV) waves on the mean stratification and circulation. A dimensional analysis may then prove a useful way to gain information about this.

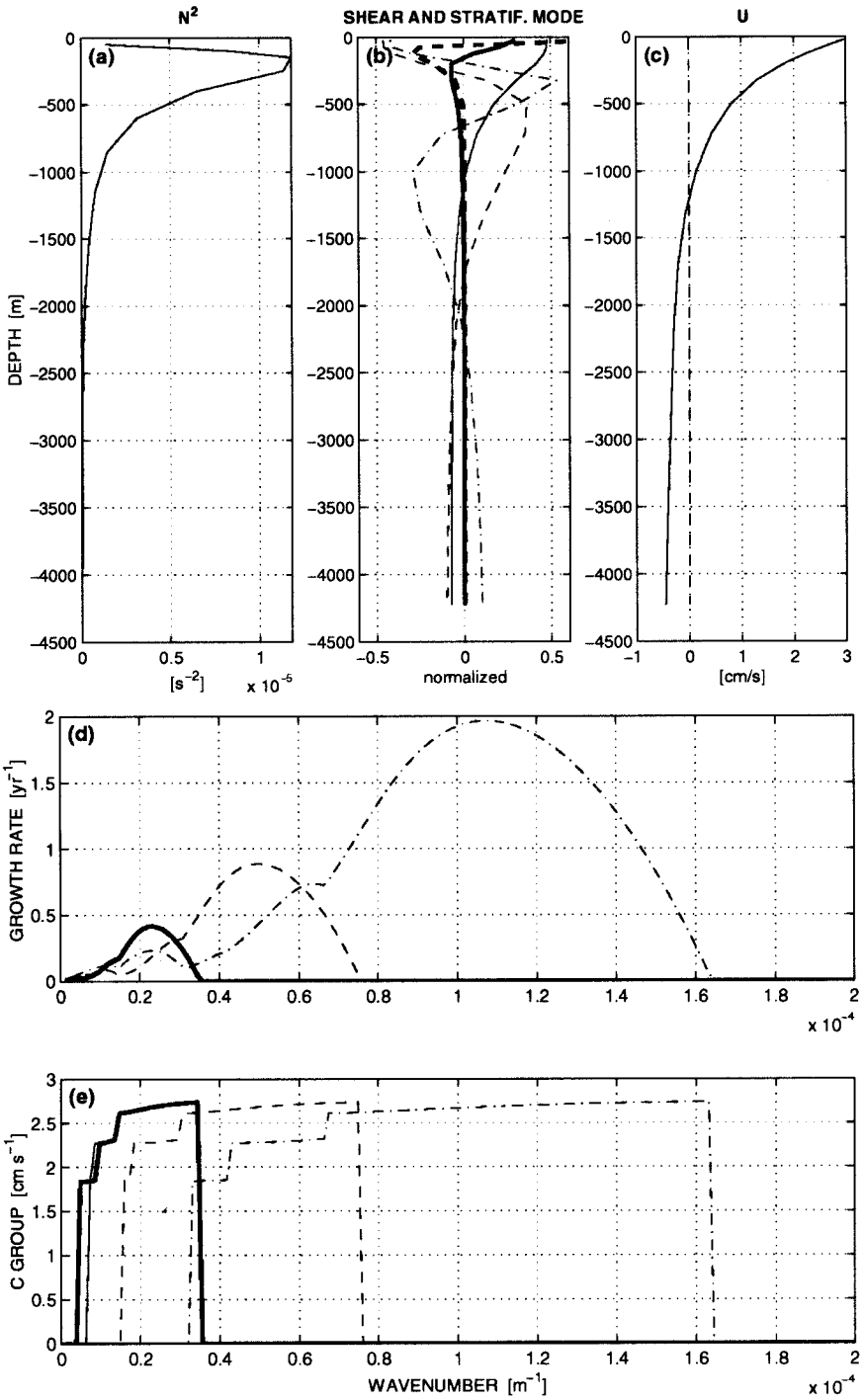

FIG. 5. Baroclinic instability calculations for the northern region of the domain from the low-resolution simulation L160. (a) Vertical profiles of the squared Brunt-Väisälä frequency and (c) the zonal velocity averaged zonally and over the northern 640 km. (b) Vertical profiles of the baroclinic stratification modes (thin: 1st, solid; 2d, dashed; 3d, dash-dotted) and the most unstable shear mode (thick: real and imaginary part respectively solid and dashed). (d) Maximum growth rate and (e) group velocity for the most unstable vertical mode as a function of the zonal wavenumber, for viscosity of 10^5 (solid), 10^4 (dashed), and 10^3 m^2 s^{-1} (dash-dotted). The thick line, for the largest viscosity but with β set to zero, often exactly superposes the solid line.

The choice of the PV waves results from a simple elimination process: as mentioned previously, neither the β effect (Winton 1996) nor frictional boundary waves are necessary for the oscillations to exist (HCW). Furthermore, these numerical boundary waves' velocity depends on the horizontal resolution (Killworth 1985) to which the oscillation period was shown to be rather insensitive (HCW). We can test that such generalized PV waves are responsible for setting the period by deriving, from simple scaling relationships, how the period depends on certain parameters and then do numerical experiments to test this. The exact propagation velocity of the PV waves on the mean stratification and circulation is intractable analytically because of the variations of both the stratification and the circulation with latitude and depth. Still, through a scaling analysis, we may try to identify which mechanism controls the propagation of the waves: a generic group velocity (first simply through the β effect) or the advection by the mean circulation (through the meridional variation of the stratification).

For both mechanisms, we derive a scaling law for the period as a function of the parameters of the model. The thermal wind and tracer balance equations give the respective scalings

$$fU/D \sim b/L_Y \quad \text{and} \tag{1}$$

$$Ub/L_X \sim B/D, \tag{2}$$

where D is the mean thermocline depth (or thickness), $b = g\Delta\rho/\rho_0$ is the buoyancy contrast related to the meridional density contrast $\Delta\rho$, U is the eastward geostrophic velocity in the thermocline, $B = g\alpha Q/(\rho_0 C_P)$ is the (given) surface buoyancy flux $O(2 \times 10^{-8}\ \text{m}^2\ \text{s}^{-3})$ derived from the maximum surface heat input Q, f the Coriolis parameter $O(10^{-4}\ \text{s}^{-1})$, and L_X and L_Y are the longitudinal and latitudinal extent of the basin $O(6 \times 10^6\ \text{m})$. It is assumed here that the thermocline depth slopes uniformly from $2D$ at 20°N to vanish at 60°N, while the meridional density contrast projects on the vertical density contrast through deep water ventilation as well as on the zonal density constrast through tracer balance and continuity.

In the absence of wind forcing, these may then be used to derive

$$U = \left(\frac{L_X B}{L_Y f}\right)^{1/2} = O(1.4\ \text{cm s}^{-1}). \tag{3}$$

Then a period based on an advective mechanism scales as

$$T_{\text{geostrophic}} = \frac{L_X}{U} = \left(\frac{L_X L_Y f}{B}\right)^{1/2}, \tag{4}$$

which is of the order of 13 yr for our standard parameters.

To evaluate the generic group velocity of the Rossby waves based on the β effect, we evaluate first the internal Rossby radius of deformation $R_d = NH/f$ with $H = D$ and $N^2 = b/D$:

$$R_d = \frac{(bD)^{1/2}}{f} = \left(\frac{UL_Y}{f}\right)^{1/2} = \left(\frac{BL_X L_Y}{f^3}\right)^{1/4}. \tag{5}$$

Then the group velocity for the Rossby waves scales as

$$C_g = \beta R_d^2 = \beta\left(\frac{BL_X L_Y}{f^3}\right)^{1/2} = O(1.7\ \text{cm s}^{-1}), \tag{6}$$

where the meridional derivative of the Coriolis parameter is $\beta = 1.6 \times 10^{-11}\ \text{m}^{-1}\ \text{s}^{-1}$. The associated travel time across the basin is then

$$T_{\text{Rossby}} = \frac{L_X}{C_g} = \left(\frac{L_X f^3}{L_Y B \beta^2}\right)^{1/2} = O(14\ \text{yr}). \tag{7}$$

This plainly applies only on the planetary scale with a meridional potential vorticity gradient given by $\partial f/\partial y$, and not for an f plane. In the presence of meridionally sloping isopycnals due to the thermodynamic forcing, the topographic β parameter based on the slope s of the thermocline scales as $fs/D = f/L_Y$, such that the topographic Rossby waves period is similar to the geostrophic scaling.

Both the advective and Rossby wave mechanisms provide similar estimation of the oscillation period in a typical parameter regime, close to the actual oscillation period in the model (25 yr). In order to identify the most satisfying mechanism, we need to go one step further and compare the parameter dependence of each estimate with the model. We analyze a series of numerical experiments from HCW over a broad parameter regime in terms of the power dependence of the oscillation period on the Coriolis parameter, the zonal and meridional extent of the basin, the buoyancy forcing, and β (see Fig. 6 and Table 1). Several planetary geostrophic models that differ in their parameterization for friction and lateral dynamic boundary conditions are used: PGL for Laplacian and no-slip, PG0 for no friction and no-slip, PGR0 for linear Rayleigh friction ($\epsilon = 4.4 \times 10^{-5}\ \text{s}^{-1}$) and no-slip, PGRW for linear friction with a vorticity closure for alongshore transport along lateral boundaries (see HWC for details). Good agreement between the model results and the scaling appears for L_X and B, which have the same exponent in both (4) and (7). The scaling we derived from the geostrophic velocities (4) (or the Rossby waves based on a ''topographic'' β effect) is in better agreement with the models for the other parameters f, L_Y, and β. This is to be expected from the calculation of the baroclinic wave velocity in the previous section, as this depends principally on the mean stratification and not on the planetary β.

In conclusion, the oscillation period scales nicely with the time it takes for a planetary wave based on the mean PV gradient (independently of the β effect) to cross the basin—this also corresponds to the zonal extent of the basin divided by the geostrophic velocity scale.

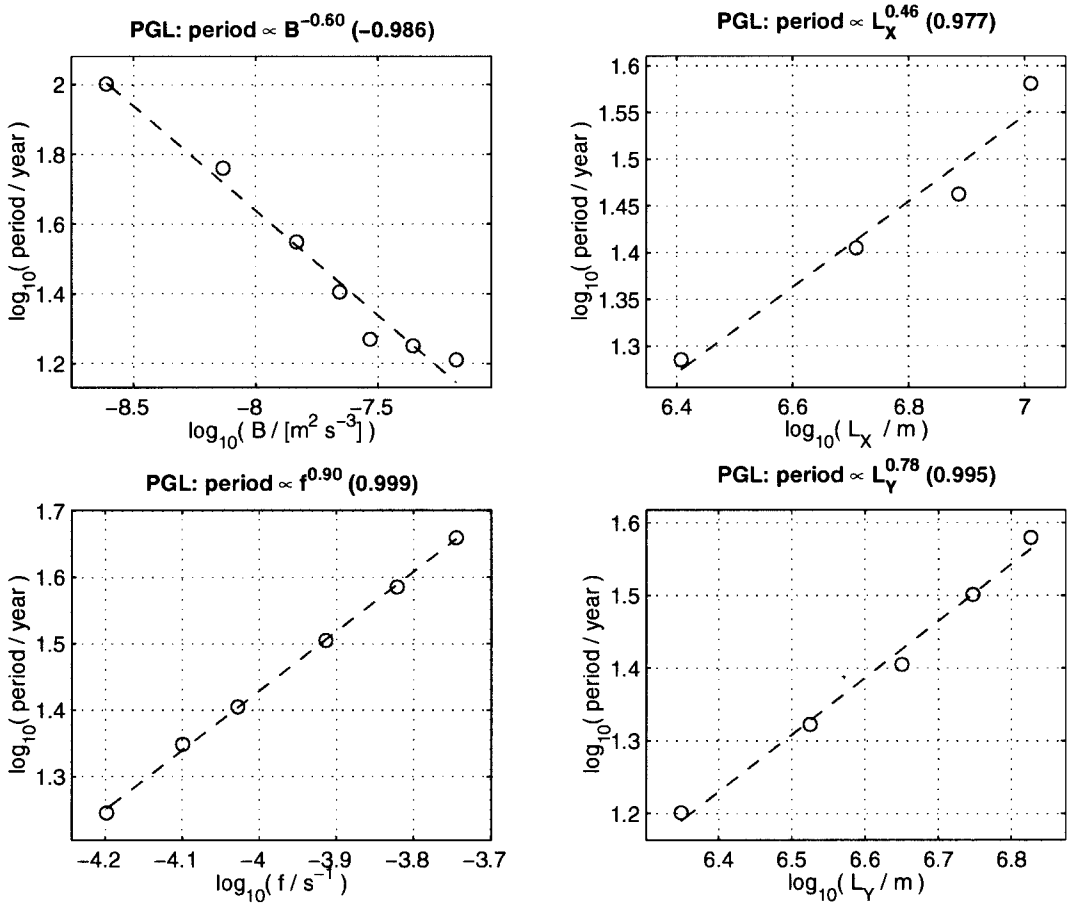

FIG. 6. Sensitivity of the oscillation period to the buoyancy forcing B, the Coriolis parameter f, the zonal and meridional extent of the basin, respectively, L_X and L_Y, in log–log plot. The circles are numerical experiments using a planetary geostrophic model with Laplacian viscosity. The dashed line is the regression line, whose slope is given in each title as the power of the parameter; the regression coefficient is given in parentheses.

3. Interaction with mesoscale turbulence

In coarse-resolution simulations the long-wave baroclinic instability has a typical growth rate of order a cycle per year. This is quite small compared to typical baroclinic instability e-folding timescales at the more traditional Rossby radius of deformation, which generates the most energetic eddies in the ocean. For example, an e-folding time of order 80 days or so for wavelength of 200 km might be typical (e.g., Gill et al. 1974). At coarse resolution, horizontal diffusion also plays an unrealistically large damping role. If baroclinic instability is indeed an energy source for interdecadal variations, we might certainly expect that the ubiquitous presence of mesoscale eddies would have a large effect, perhaps on both the period and amplitude of the oscillations, perhaps even on their existence. This issue is examined by refining the resolution in an ocean model in order to actually resolve the most energetic structures that are responsible for the large-scale mixing of tracers and momentum. The choice of subgrid-scale parameterization is not eliminated, merely shifted to smaller scales, and might still be influential on the global features of the circulation. Given our achievable numerical resolution, we choose to use a scale-selective biharmonic operator, enabling us to reach a higher and more

TABLE 1. Power law of the oscillation period as a function of the Coriolis parameter f (at midbasin on a β plane centered at 40°N), the zonal and meridional extent of the ocean basin L_X and L_Y, the buoyancy forcing amplitude B and β (f remaining fixed at 40°N); note that there is no wind forcing in these experiments. Power laws are given for various models simulations (HCW), and for the geostrophic scaling in terms of PV wave propagation on the mean stratification and circulation, and the generic Rossby wave propagation based on constant planetary β.

Power law	f	L_X	L_Y	B	β
PGL	0.90	0.46	0.78	−0.60	0.10
PG0	0.64	0.62	0.95	−0.65	0.23
PGR0	0.80	0.34	0.82	−0.67	0.13
PGRW	0.82	0.44	0.36	−0.50	−0.32
Models average	0.79	0.47	0.73	−0.61	0.03
$T_{\text{geostrophic}}$	1/2	1/2	1/2	−1/2	0
T_{Rossby}	3/2	1/2	−1/2	−1/2	−1

TABLE 2. Summary of low- to high-resolution experiments. Experiment label: horizontal momentum and tracer diffusion operator (*L* for Laplacian, *B* for biharmonic), horizontal resolution (km). Time series: integration time for statistics (year). Parameters A_H, K_H: momentum and tracer horizontal diffusion coefficients [($m^2\ s^{-1}$) for Laplacian, ($m^4\ s^{-1}$) for biharmonic]. KE density: total kinetic energy density, mean, and standard deviation (0.1 kg $m^{-1}\ s^{-2}$). SST: mean surface temperature (upper 50 m), mean and standard deviation (°C). Tbot: time-averaged mean bottom temperature (lower 550 m) (°C). PHT: advective poleward heat transport, mean, and standard deviation (PW). The oscillation period is regular in the lower-resolution case, while a second peak appears in the spectral analysis of the higher-resolution cases (both most energetic periods are then given separated by "+").

Expt Δ_{xy} (km)	Time series (year)	Parameters		KE density		SST		Tbot	PHT		Oscillation period (year)
		A_H (m^n/s)	K_H (m^n/s)	Mean (0.1SI)	Stdev (0.1SI)	Mean (°C)	Stdev (°C)	Mean (°C)	Mean (PW)	Stdev (PW)	
L320	1000	6e5	1000	0.162	0.018	13.807	0.110	3.318	0.264	0.025	25.5
L160	1000	1.5e5	700	0.262	0.045	13.643	0.095	3.187	0.254	0.025	26.0
L80	200	1e4	500	0.563	0.095	13.096	0.075	3.144	0.251	0.024	27.0
L40	200	1e3	250	1.183	0.363	13.331	0.299	3.094	0.265	0.044	25 + 50
B40	200	*2e11*	*2e11*	3.298	1.368	15.142	0.240	3.100	0.267	0.057	22 + 55
L30	100	450	150	1.682	0.420	12.806	0.152	3.256	n/a	n/a	20 + 43
B30	100	*1e11*	*1e11*	11.737	5.681	13.155	0.178	3.205	0.268	0.043	21 + 34
L20	100	100	100	6.352	1.439	12.782	0.117	3.251	0.282	n/a	24 + 37
B20	200	*4e10*	*4e10*	44.417	3.204	13.647	0.085	3.231	0.289	0.029	33 + 44

realistic level of turbulent kinetic energy than is achievable with a Laplacian viscosity.

a. Model setup

A first estimate of the scale of eddies is simply the deformation radius, which is obtained as solutions of the quasigeostrophic eigenvalue problem:

$$\frac{d}{dz}\left(\frac{f^2}{N^2}\frac{d\psi}{dz}\right) = \lambda^2\psi, \tag{8}$$

where λ is the eigenvalue. Results from our coarse-resolution simulations indicate that the first baroclinic Rossby radius of deformation ($R_d = 1/\lambda$) is about 13 km in the polar regions, going to about 34 km in the tropical regions. Resolving this first mode (a minimum requirement for any putative "eddy permitting" simulation) requires at least a resolution of 20 km, in order to have a few grid points within a typical eddy diameter ($\sim 2\pi R_d$ perhaps).

This resolution is achieved using a suite of numerical experiments with the Modular Ocean Model (Pacanowski et al. 1991), within the same idealized geometry and forcing as section 2, and no wind forcing. The use of zonally uniform constant surface fluxes of heat depending only on latitude keeps the forcing independent of the ocean dynamics, such that no implicit zonal structure might interfere with the western boundary current. The vertical discretization as well as uniform vertical mixing of tracer ($10^{-4}\ m^2\ s^{-1}$) and momentum ($10^{-3}\ m^2\ s^{-1}$) is kept independent of the resolution.

The horizontal resolution is progressively increased from 320, 160, 80, 40, 30, and 20 km, while horizontal mixing parameterization (Laplacian or biharmonic) and coefficients are correspondingly reduced (see Table 2). Each new resolution is initialized with a bilinear interpolation of the previous field after a sufficiently long integration for the deep-water properties to be statistically constant. The first phase of the spinup is carried with asynchronous time steps for temperature and velocities, while the second phase uses synchronous time steps (this synchronicity has a significant influence on the mesoscale variability at high resolution). The model is then integrated synchronously for a minimum of 200 yr, during which the statistics are computed (Table 2). If a biharmonic diffusion is used, it is initialized from the Laplacian simulation for the same resolution and follows the same adjustment procedure.

In a closed basin, the adjustment timescale of the mean circulation when parameters, parameterization, or resolution are changed is at least of the order of a baroclinic Rossby wave travel across the basin at 60°N, around 20–30 yr. This became especially clear when spinning-up the 20-km resolution biharmonic simulation from the 20-km Laplacian one. Over a 35-yr period, the mean basin turbulent kinetic energy kept rising (reaching more than 5 times its harmonic value) while the mean sea surface temperature increased by almost 1°C.

b. Results

Over simulations with about an order of magnitude change in the horizontal resolution, the total kinetic energy was found to vary by more than two orders of magnitude, while the mean kinetic energy (based on time-averaged velocities) varied by at most a factor of 2. The most significant jump in eddy kinetic energy (EKE) arose with the use of biharmonic mixing of momentum and tracer for resolutions of 40 km and higher. (In fact the Laplacian friction allows very few "eddies" even at the 20-km resolution; see Table 2.) Sea surface height variability reaches values of 30 cm (rms) on long timescales along the western boundary and its extension in the eastward jet along 55°N, while the lowest values (4 cm) are achieved in the tropical and southeast area (not shown). This is broadly consistent with estimates

from satellite altimeters, reaching values of the order of 34 cm in the Gulf Stream region (Stammer and Böning 1992). On shorter timescales more relevant for the mesoscale turbulence, the sea surface height variability amounts to 14 cm in the western boundary current region (peaking at 40°N). Without any wind forcing, we thus achieve a reasonable amount of EKE for a 20-km biharmonic run, which should resolve realistically the mixing of tracer and momentum by mesoscale eddies.

There is no systematic trend in the mean circulation diagnostics with increasing resolution, whether one looks at mean surface or bottom temperature, meridional overturning, or poleward heat transport. This seems likely to be a consequence of the fixed flux boundary conditions applied that constrain the total heat transport, which, in turn, is dominated by advection. However, there is a radical change in the mean circulation structure with increasing resolution. Comparing the time-averaged temperature field in the upper 50 m for the 20 km biharmonic simulation (Fig. 7a) to the 160-km Laplacian simulation (Fig. 2a), the western boundary current shows a much-reduced northern extent and a broader structure, while the cold regions due to the upwelling along the western boundary have vanished. Significant differences appear also in the northeast corner where northward sloping isotherms in the eddying case replace the purely zonal jet hitting the wall at coarse resolution: a cyclonic circulation reduces the cross-isopycnal sink of waters along the eastern boundary and shifts the coldest deep waters westward along the northern boundary. The meridional gradient of density has decreased overall with higher resolution, mainly because lower temperatures are achieved in the tropical region.

There is also little systematic trend in the amplitude of the variability of most of the diagnostics with changing resolution (see Table 2). These integral variables evolve on the interdecadal timescale with an amplitude much larger than on the eddies timescale and, with one notable exception, this long-term amplitude does not change significantly with the resolution. The exception is that on the interdecadal timescale, the total kinetic energy varies with an amplitude roughly proportional to its mean value (between 10% and 50%, see Fig. 8b). The EKE (representing most of the total kinetic energy) is intrinsically based on the mesoscale features, with typical timescales of a few months. The large variation of the envelope of this activity on interdecadal timescales suggests that the various states through which the model evolves over decades are fundamentally different in terms of potential energy that can be released through baroclinic instability. This is at least consistent with the notion that baroclinic instability is an important factor producing the variability at both low and high resolution. Comparing the time evolution of KE and surface temperature at high and low resolution (Fig. 8 vs 1), the asymmetry between the increasing and decreasing phase is more pronounced at high resolution, similar to the evolution of meridional overturning or poleward heat transport at low resolution. Our interpretation is that the overturning circulation slowly builds up until the circulation is so intense that the release of potential energy peaks, then the circulation breaks down within years and the oscillation starts anew.

Describing the pattern of variability in the eddying experiments is more complex and costly than at lower resolution: not only does the local amplitude of temperature anomalies due to eddies easily exceed the long-term variations, but numerous very energetic events of zonal jets bursting eastward out of the western boundary current strongly perturb the mean temperature field. Annual averages of the temperature fields would have helped greatly, but were not performed during the integration to save memory usage. In order to filter out as efficiently as possible the mesoscale patterns in annual snapshots of the temperature, and also to reduce the size of the fields to analyze, we perform a horizontal averaging over eight grid points in both latitude and longitude—the grid is now similar to the L160 experiment. An EOF analysis is conducted in the same manner as in section 2b; that is, on the full three-dimensional temperature fields taken every year for 90 yr. The first two EOFs representing, respectively, 29% and 17% of the variance and varying in quadrature on a 45-yr timescale are shown in Fig. 7. Their structure is significantly different than the low-resolution patterns (Fig. 2), although some similarities may be found in their large-scale features. A major difference is the zonal jetlike structure along 50°N, which is unique to the experiment with energetic mesoscale variability; with an intense signature but narrow extent in latitude, it cuts through the largest-scale temperature anomalies situated in the northern half of the domain.

We also performed a composite analysis, by averaging the temperature fields for all the years with KE and SST higher than the time average plus the standard deviation, then for all the years with KE and SST lower than the time average minus the standard deviation, and taking the difference of these two fields: we obtain a pattern very similar to EOF 1 with amplitude 3 and -1.5°C. The same analysis performed at low resolution (exp. L160) looked very much like the opposite of EOF 2 (Fig. 2c). The high-resolution pattern looks quite different, and this is likely related to the different dynamics and path of the western boundary current, as acknowledged in the previous comparison of the mean circulation.

Let us now address the issue of the regularity of the long-term variability. While the low-resolution simulations produce quite regular monochromatic oscillations (even sinusoidal for the lowest resolution) of the diagnostics as a function of time, which makes them perfectly predictable, the regularity is lost for resolution of 40 km and higher. The time series now contain small amplitude oscillations on infra-annual to interannual timescales, and we systematically observe a second peak in the spectral domain, at roughly twice

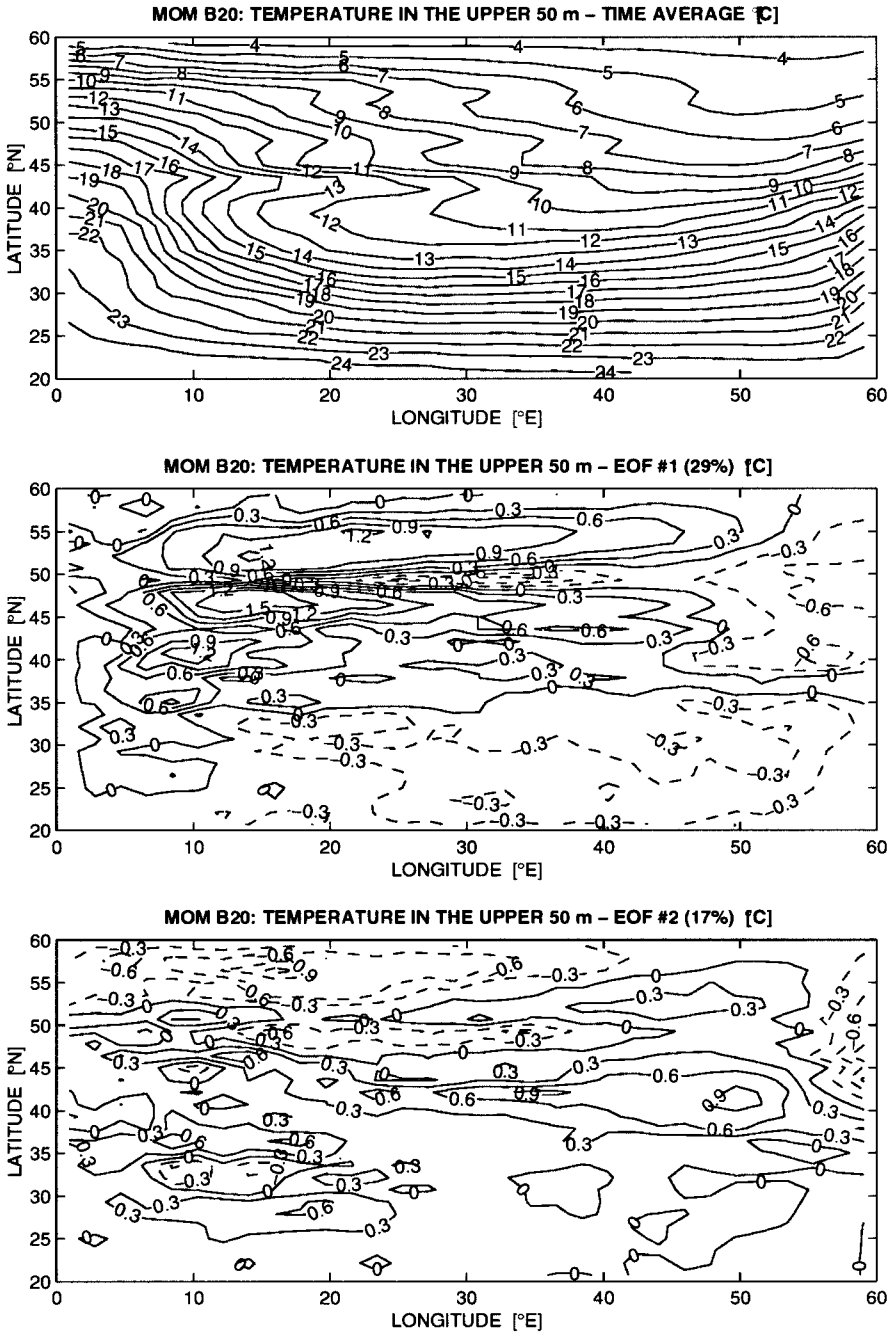

FIG. 7. Temperature in the upper 50 m for the highest-resolution experiment (B20): (a) time average, (b) first, and (c) second EOF. The EOF analysis is performed on annual snapshots of the three-dimensional temperature fields that are horizontally averaged on a lower-resolution grid (L160). A composite analysis, differentiating the surface temperature at times with high vs low surface temperature and kinetic energy, shows a structure very similar to EOF 1, with amplitude of up to 3° and −1.5°C.

the main period of oscillation. The most energetic peak remains in the 20- to 35-yr range periods for most simulations, while the second peak appears at 35- to 60-yr periods. Only in the B20 experiment the most energetic peak is at approximately 44 yr. Although our 200-yr-long time series are too short for statistical robustness, the consistent presence of these longer periods certainly deserves further study. Based on recent three-dimensional linear stability analysis of the circulation, our interpretation is that planetary waves with

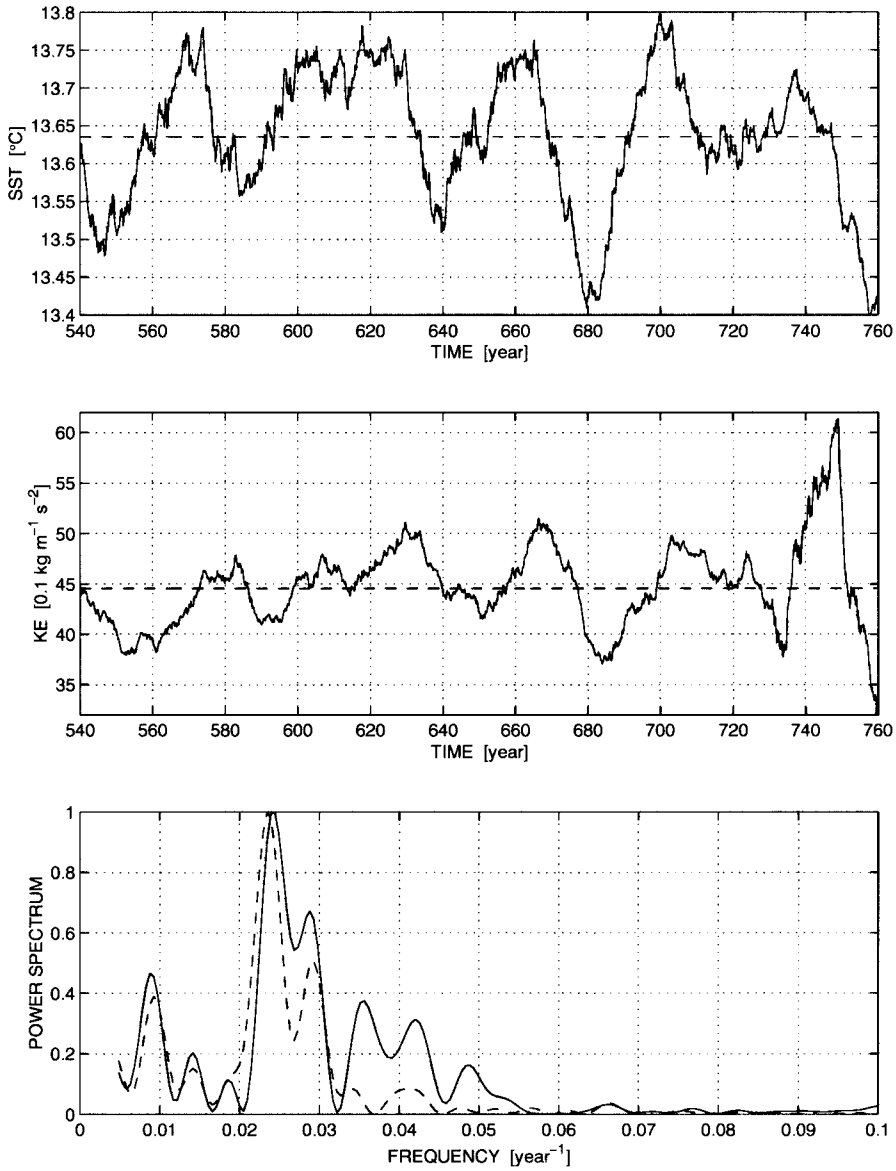

FIG. 8. Time series of (a) mean surface temperature and (b) total kinetic energy for the 20-km resolution experiment with biharmonic mixing of heat and momentum (B20); (c) power density spectra for total kinetic energy (solid) and mean sea surface temperature (dashed).

higher zonal wavenumber become unstable when dissipation gets lower at higher resolution. These propagate with different speed and produce additional peaks in the variability spectrum.

The most fundamental result from this series of experiment is the robustness of the interdecadal variability to the mesoscale turbulence. Fanning and Weaver (1998) have already shown that higher resolution and associated reduced diffusion makes interdecadal oscillations more likely to occur. We have found here that the eddy activity does not change systematically the characteristics of long period variability already present at coarse resolution. However, the mesoscale turbulence clearly perturbs the regularity of the oscillations, which is likely to make them less predictable.

4. Coupling with a simple atmosphere

a. The atmospheric energy balance model

The boundary conditions we have used thus far, constant flux, are rather special and in many regards unrealistic, especially in that they do not allow the meridional heat transport of the ocean to vary. To investigate the potential importance of this in the production of long-term oscillations, we use a two-dimensional,

energy balance atmospheric model (EBM) to provide surface boundary conditions. Sensible heat exchange with the atmosphere is likely to act as a damping factor in any oscillatory motion. If an effective ''air–sea coupling coefficient'' is sufficiently large the associated damping may be sufficient to kill the oscillations, as for example, in Chen and Ghil (1996, CG96 hereafter) who found a critical value of about 25 W m^{-2} K^{-1}. We might hypothesize that if surface density anomalies are damped on timescales shorter than the *e*-folding timescale of long-wave baroclinic instability O(cycle/year), the oscillations will not be sustained. Recent estimations of an appropriate value for such an exchange coefficient vary widely from 10 W m^{-2} K^{-1} (Seager et al. 1995) to more than 65 (Chu et al. 1998), and indeed no single value really exists because of its dependence on surface wind speed. This section constitutes an exploration of these issues: We use a two-dimensional EBM coupled to our planetary geostrophic ocean model in spherical coordinates, and no wind forcing. In contrast with Chen and Ghil (1996) experiments, we distinguish the flux into the ocean into the solar short-wave absorption, which does not depend on the SST, and the sensible heat.

The formulation of our EBM uses relatively standard parameterizations of solar and infrared flux, linear terms representing the exchange of sensible heat between ocean and atmosphere, and the lateral transfer of heat within the atmosphere parameterized by uniform diffusion. Salinity in the ocean, and water vapor in the atmosphere (along with latent heat), is neglected. The governing equations for the atmospheric temperature may be written

$$C_A \frac{\partial T_A}{\partial t} = Q_{\mathrm{SA}} - Q_{\mathrm{LWA}} + Q_{\mathrm{RR}} + Q_{\mathrm{SH}} + C_A \boldsymbol{\nabla} \cdot (K_A \boldsymbol{\nabla} T_A), \quad (9)$$

$$Q_O = Q_{\mathrm{SO}} - Q_{\mathrm{RR}} - Q_{\mathrm{SH}}, \quad (10)$$

$$Q_{\mathrm{RR}} = \epsilon_O \sigma T_O^4 - \epsilon_A \sigma T_A^4, \quad (11)$$

$$Q_{\mathrm{LWA}} = A_L + B_L T_A, \quad \text{and} \quad (12)$$

$$Q_{\mathrm{SH}} = \gamma (T_O - T_A), \quad (13)$$

where $T_A(x, y, t)$ and $T_O(x, y, t)$ are the atmospheric temperature (some vertically integrated value) and sea surface temperature, respectively. Here, Q_{SA} is the net solar radiation absorbed in the atmosphere; Q_{LWA} is the net long-wave (infrared) emission to space; Q_{RR} is the long-wave radiation emitted from the surface, all of which is assumed absorbed in the atmosphere; Q_{SH} is the sensible heat exchange between ocean and atmosphere. The last term in (9) represents the lateral exchange of heat in the atmosphere, Q_{SO} represents the net solar radiation absorbed by the ocean, and Q_O thus represents the net heat input into the ocean.

The incoming solar radiation depends only on latitude (following Chyleck and Coakley 1975), with a uniform albedo of 0.3. The atmosphere absorbs 30% (Q_{SA}) of the net incoming solar radiation, while the ocean absorbs the remaining (Q_{SO}). Emission and absorption of infrared radiation between ocean and atmosphere (Q_{RR}) follow a simple graybody law, with oceanic and atmospheric emissivity of $\epsilon_O = 0.96$ and $\epsilon_A = 0.85$, respectively. The atmospheric upward emission of infrared radiation Q_{LWA} follows a Budyko-type linear relation ($A_L = 210$ W m^{-2} and $B_L = 2.0$ W m^{-2} K^{-1}). (The form of these parameterizations is not crucial; e.g., purely linear terms could have been used for Q_{RR} with little difference.) The exchange of sensible heat between ocean and atmosphere is linearly related to the difference of the temperatures between the atmosphere (T_A) and the first level of the ocean model (T_O) through the exchange coefficient γ, taken as uniform since there is no wind. The atmospheric heat capacity is set to $C_A = 10^7$ J m^{-2} K^{-1}, horizontal transports of heat are parameterized by an eddy-diffusion $K_A = 10^6$ m^2 s^{-1}, with a no-flux boundary condition applied on the lateral boundaries.

These experiments are implemented in a domain extending from 10° to 70°N and 60° wide. This larger meridional extent is necessary to get realistic north–south temperature contrast and overturning rate, since we no longer have control on the extreme sea surface temperatures with the EBM. The ocean basin is 4500 m deep with the same vertical discretization and mixing coefficients as section 2 ($K_V = 10^{-4}$ m^2 s^{-1} for tracers). The horizontal resolution is 2° and horizontal mixing coefficients are, respectively, 10^3 m^2 s^{-1} for tracers and 10^5 m^2 s^{-1} for momentum. The wind forcing is set to zero in these sensitivity experiments. The exchange coefficient γ is varied between 0 and 65 W m^{-2} K^{-1} and various diagnostics are computed over 1000 yr following a 4000 yr spinup from rest. The oscillations are perfectly regular for all these experiments, with significant amplitudes and similar periods. Figure 9 shows the mean and standard deviation of the sea surface and atmospheric temperatures as well as the air–sea heat flux. In the absence of zonal winds in the atmosphere, changes in temperature O(0.5°C) and surface flux O(16 W m^{-2}) follow closely the upper-ocean variability O(0.8°C) intensified in the northwest quarter. Because of the large atmospheric eddy diffusion, temperature anomalies are never as large as in the upper ocean and the surface fluxes (positive into the ocean) are in opposition of phase with the SST, resulting in a damping of the anomalies but much smaller than if the atmospheric temperature was fixed.

b. Results

Results show clearly that for this configuration where the vertical diffusivity is relatively high ($K_V = 10^{-4}$ m^2 s^{-1}), the exchange coefficient does not play a critical role on the variability (Fig. 10). The oscillation ampli-

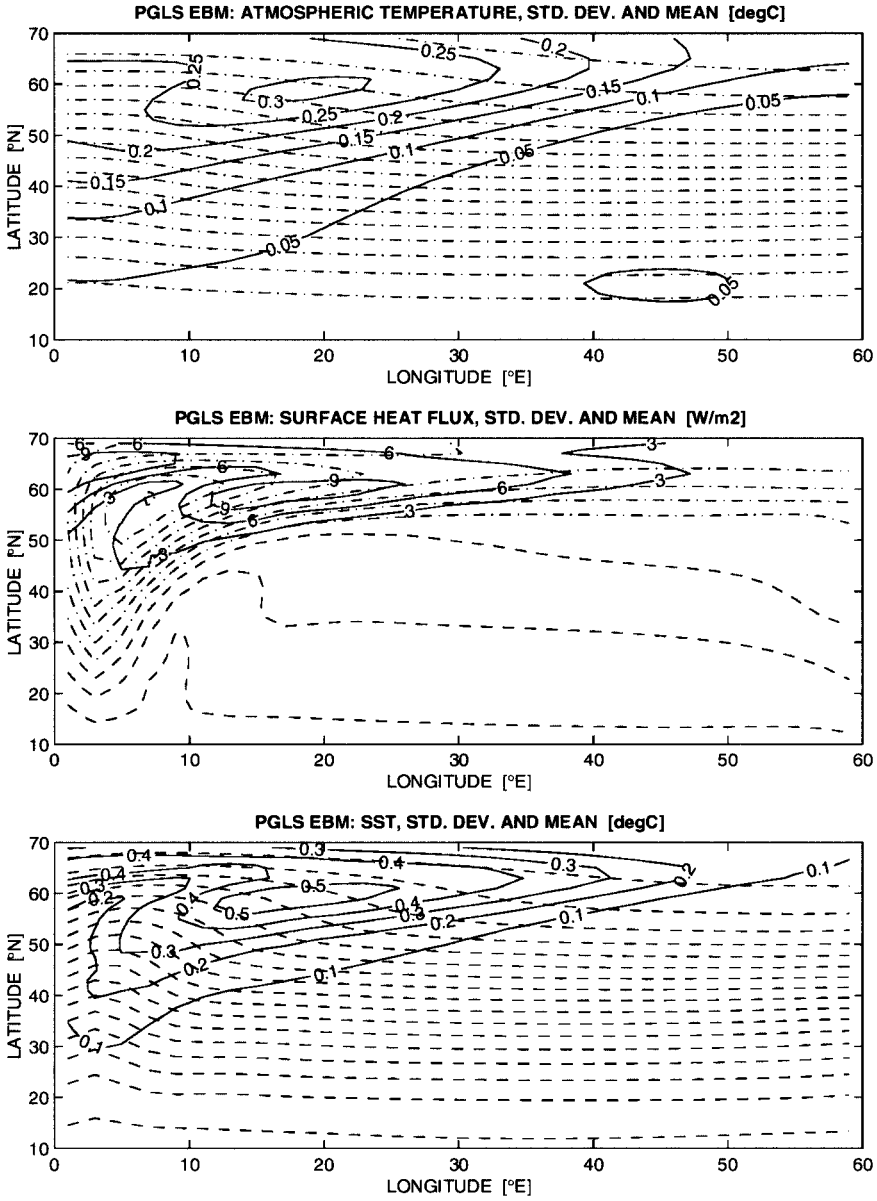

FIG. 9. Standard deviation (solid contours) and time average (dashed contours) of (a) atmospheric temperature (°C), (b) surface heat flux (W m^{-2}), and (c) sea surface temperature (°C) in the ocean model coupled to an atmospheric energy balance model. Here the albedo is constant, the exchange coefficient is 35 W m^{-2} and the vertical diffusion is 10^{-4} m^2 s^{-1}.

tude, as seen in the standard deviation of kinetic energy or mean sea surface temperature, decreases with increasing γ, while the mean circulation gets slightly more energetic. However, the oscillations are always sustained with periods increasing from 33.8 to 40.3 yr with γ. In fact, the coupling coefficient modifies primarily the lowest temperature achieved at the ocean surface, thus the deep-water temperature: the mean bottom water temperature decreases from 23.7°C for $\gamma = 0$ to 4.2°C for $\gamma = 65$.

However, for smaller (perhaps more realistic) vertical diffusivity, the presence of long-term oscillations depends quite sensitively on the exchange coefficient with the atmosphere. Using $K_V = 0.5 \times 10^{-4}$ m^2 s^{-1} we now find that the oscillations are only sustained for a narrow range of exchange coefficients ($\gamma = 15$ to 20 W m^{-2} K^{-1}), while the model settles into a steady state for a lower or larger exchange coefficient. Note that it takes 3000 yr or more for the oscillations to die out in most of the cases, so that the real climate system would certainly still be oscillating given the synoptic, seasonal, and interannual changes in the atmospheric forcing. For still smaller values of the vertical diffusivity, self-sustained oscillations are not found.

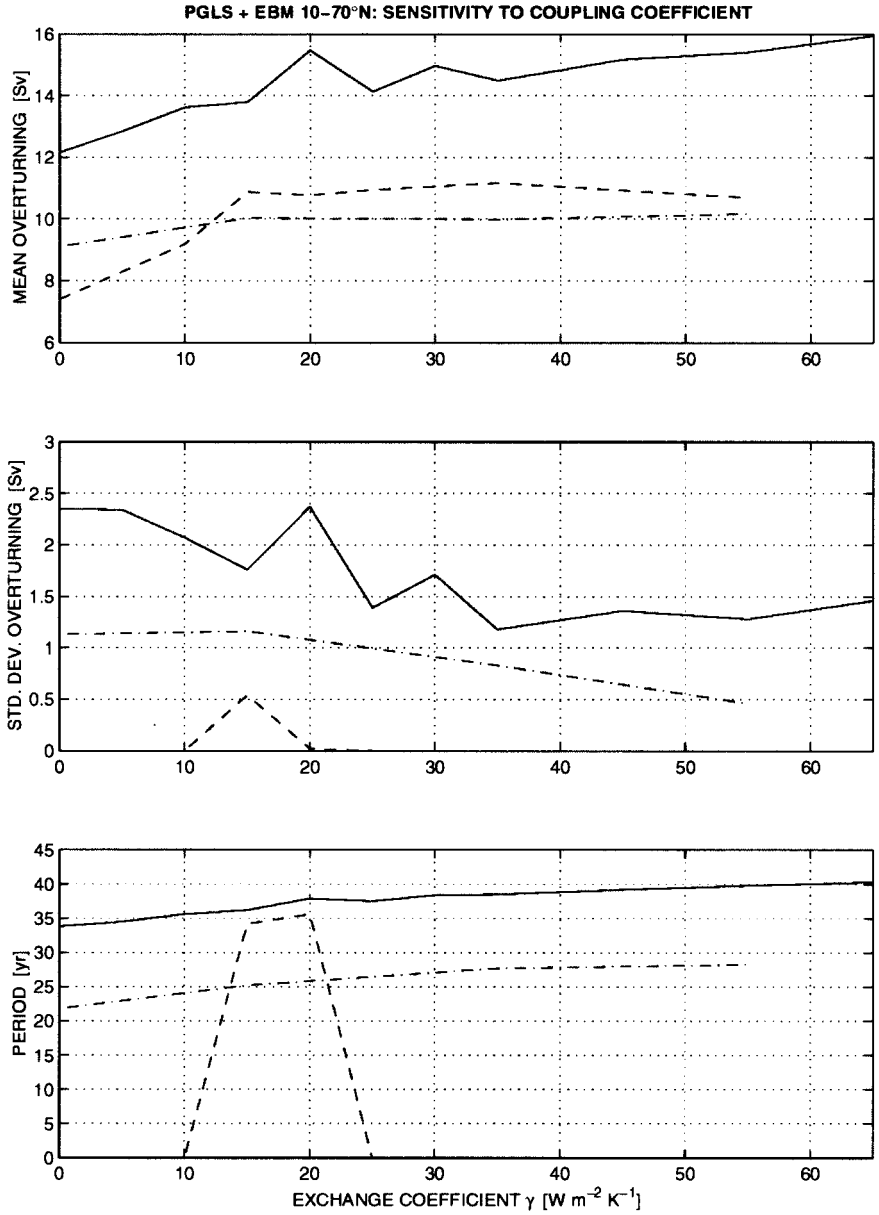

FIG. 10. Sensitivity to the coupling coefficient for the simulations with a planetary geostrophic model in spherical coordinates with Laplacian viscosity coupled to an atmospheric energy balance model, in a flat-bottom basin extending from 10° to 70°N and 60° wide. (a) Mean and (b) standard deviation of the maximum overturning streamfunction, and (c) oscillation period, as a function of the coupling or exchange coefficient, for vertical tracer diffusivities K_V of 10^{-4} (solid line) and 0.5×10^{-4} m^2 s^{-1} (dashed line) with constant top-of-the-atmosphere albedo (0.3). With a more realistic top-of-the-atmosphere albedo $\alpha = 0.20 + 0.36 \times \sin^2$(latitude), the oscillations are more robust even for $K_V = 0.5 \times 10^{-4}$ m^2 s^{-1} (dash-dotted line).

Finally, we reproduce the low vertical mixing experiments but imposing a larger meridional temperature contrast through a larger differential solar short-wave flux. The warm deep water temperatures obtained so far pointed out a weakness in the EBM parameterization, namely, the constant albedo with latitude. Due to the higher reflectivity of the incoming shortwave radiations entering the atmosphere at higher latitude, Graves et al.'s (1993) analysis of satellite data suggests to use for the top-of-the-atmosphere annual-mean albedo: $\alpha = 0.20 + 0.36 \sin^2(\theta)$, where θ is the latitude [actually a small term in $\sin(\theta)$ is omitted from their coefficients for symmetry]. The bottom waters now reach cooler more realistic temperatures, but most importantly, the oscillations are now sustained throughout the range of variation of the exchange coefficient.

These series of experiments illustrate the two competing influences of γ on the variability. First, the exchange coefficient modifies the extreme temperatures achieved at the surface, hence the mean stratification and circulation. And through a larger stock of available potential energy, instabilities are more likely to grow. But γ also damps the surface temperature anomalies by restoring them to the atmospheric temperatures. Indeed, by reducing γ from 65 to 0 W m^{-2} K^{-1}, the effective damping of the SST anomalies can be reduced by a factor of 2 (see CVH). The overall picture is then as follows: for sufficiently large vertical mixing or differential heating, the thermohaline circulation is strong enough that, over a wide range of γ, it is unstable: the instability growth rate overcomes the damping role of sensible heat fluxes. (The first set of experiments shows indeed a decrease in the oscillations amplitude with increasing γ, although the intensity of the overturning is increasing.) For low vertical mixing and constant albedo, the overturning is too weak to develop any instability even for small γ. For increasing γ, the meridional temperature gradient becomes large enough to drive an unstable thermohaline cell, and γ is still weak enough to let it settle into decadal oscillations. However, for larger γ, the damping role overcomes the instability growth rate and the model settles into a steady state. With varying top-of-the-atmosphere albedo, the enhanced differential heating drives a more intense thermohaline circulation such that the instability overcomes the damping role of the sensible heat exchange with the atmosphere.

c. Baroclinic instability growth rate

If a slow, long-wave baroclinic instability is the energy source for the long-term oscillations, then an analysis of the baroclinic instability of the mean state in an oscillating case and a nonoscillating case should reveal marked differences. We choose to compare two states with the same exchange coefficient (35 W m^{-2} K^{-1}), under the original forcing with constant albedo, one with large vertical mixing that drives oscillations, one with reduced vertical mixing that leads to a steady state.

We use the local quasigeostrophic calculations, as described in section 2, with the actual viscosity of the planetary geostrophic model. We apply the computation to the vertical profiles of the time-averaged density and velocity for each horizontal grid point of the model, and map largest growth rate over wavenumber and wave direction (Fig. 11). Although there are no qualitative differences between the maps of growth rate for $K_V = 10^{-4}$ and 0.5×10^{-4} m^2 s^{-1}, the former shows larger values in the northwest region where the variability is usually intensified. Largest growth rates are usually found in the northeast corner where the meridional shear is large while the stratification is weak. However, it is not clear which unstable region is actually feeding the variability (and this might also be a function of time). Overall, the linear growth rate calculations do support the notion that the circulation and stratification is more unstable when K_V is larger, and that this then sustains the interdecadal oscillations—but maybe it is just fortunate that the local instability calculation on the time mean state matches here the global instability growth rate.

5. Interaction with the wind-forced circulation

a. Numerical experiments

As is well known, the addition of wind forcing profoundly alters the circulation of the upper ocean. Indeed, the structure of the thermocline is at least in part determined by wind forcing. Its effect on the thermohaline circulation is more subtle (see, e.g., Vallis 2000). In this section we perform a preliminary study of how wind forcing affects the longer-term variability of the thermohaline circulation.

A first series of experiments is set in the standard Cartesian geometry (section 2, experiment L160), by adding a wind-forced circulation of increasing intensity. Constant heat flux continues to provide the thermodynamic forcing. The wind stress is simply zonal and function of latitude according to the analytical formula of Bryan (1987), close to the North Atlantic annual-mean climatology: it is multiplied by a factor ranging from 0 (pure thermal forcing) to 3, by increments of 0.5. For the standard wind, the interaction of the barotropic circulation with the thermohaline cell does not perturb considerably the variability, that even increases slightly. Results are summarized in Table 3 and Fig. 12.

Whereas the maximum overturning circulation increases with the wind forcing, the variability remains quite unperturbed until the wind stress reaches 1.5 times the climatological value, then it decreases rapidly and disappears for coefficients of 2.5 and 3. The oscillation period keeps decreasing slightly with increasing wind (from 25.4 to 22.7 yr) until the oscillations disappear. The influence of the wind forcing appears to become critical when the intensity of the Ekman pumping is larger (in an appropriate sense) than the value of the thermal forcing. This can be expressed in terms of the strengths of the vertical velocities induced by advective–diffusive effects, and by Ekman pumping, respectively, namely, $W_{\mathrm{TH}} = K_V/D$ (where D is a vertical scale associated with the thermocline) while $W_E = \boldsymbol{\nabla} \times \tau/(f\rho_0)$. Thus, a critical value for the strength of the Ekman pumping arises when $W_{E(\mathrm{crit})} = K_V/D$. Although D itself varies with both wind and diffusivity, the dependence in both cases is to some fractional power (e.g., Vallis 2000). Thus, wind effects will be relatively more important if the vertical diffusion is small. Now, the experiments above used a relatively large vertical diffusion coefficient for heat (10^{-4} m^2 s^{-1}). If the vertical diffusion coefficient is reduced to 0.5×10^{-4} m^2 s^{-1}, the oscillations are sustained for wind factors 0–2 but not

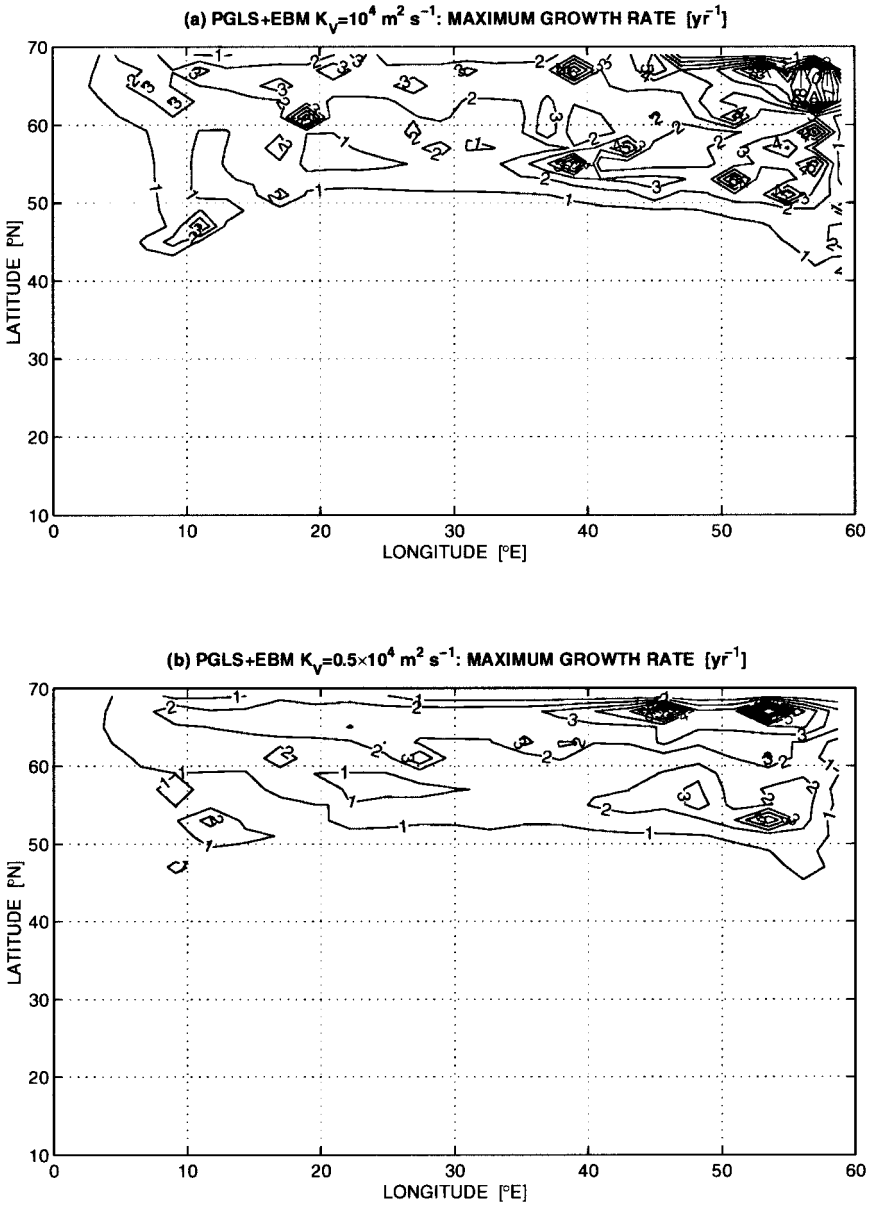

FIG. 11. Maximum baroclinic instability growth rate (yr^{-1}) for one oscillating configuration ($K_V = 10^{-4}$ m^2 s^{-1}) and one steady state ($K_V = 0.5 \times 10^{-4}$ m^2 s^{-1}) of the planetary geostrophic model coupled to the atmospheric energy balance model with the same exchange coefficient (35 W m^{-2}). The time-averaged vertical profiles of density and zonal and meridional velocities were used, with the Laplacian viscosity from the ocean model (10^5 m^2 s^{-1}).

for 3, qualitatively consistent with this notion. Figure 13 shows that the variability is indeed significantly enhanced for the climatological wind forcing but severely reduced for stronger winds. Its structure is also shifted toward the western boundary current region until it totally disappears. Note that in all these cases, the zero-wind stress line is around 45°N.

b. Interpretation

One might expect that the damping influence of the wind forcing on the variability will be related to the change it induces on the mean circulation. That is to say, the mean circulation under three times the climatological wind would be less unstable in terms of long-wave baroclinic instability. This does not appear to be the case. We again perform a linear quasigeostrophic baroclinic instability growth rate calculations for the vertical profiles of density and horizontal velocity. We compute the maximum growth rate of instability at each horizontal location for the time averaged circulations for 0, 1, 2, and 3 times the climatological wind forcing. It appears that the large vertical shear induced by the

TABLE 3. Sensitivity to the wind forcing (experiment L160). First (second) series of experiment is for high (reduced) vertical mixing rate, $K_V = 10^{-4}$ (0.5×10^{-4}) m^2 s^{-1}. Experiments W_E use a constant Ekman pumping through a wind stress linearly varying with latitude, while $\underline{W_E}$ use in addition the opposite heat flux. Wind factor: multiplying the analytical wind stress of Bryan (1987). Oscillations period (yr). Total kinetic energy, mean, and standard deviation (0.1 kg m^{-1} s^{-2}). Maximum of the advective poleward heat transport (PHT), mean and standard deviation (PW). Horizontally averaged sea surface temperature (SST), mean and standard deviation (°C).

		Total KE		PHT		SST	
Wind factor	Oscillation period (year)	Mean (0.1SI)	Stdev (0.1SI)	Mean (PW)	Stdev (PW)	Mean (°C)	Stdev (°C)
0.0	25.4	0.286	0.046	0.254	0.025	13.774	0.091
0.5	25.4	0.431	0.070	0.257	0.032	13.098	0.081
1.0	25.1	0.668	0.097	0.253	0.041	12.744	0.077
1.5	23.9	0.993	0.118	0.251	0.038	12.299	0.061
2.0	22.7	1.397	0.036	0.246	0.009	11.699	0.011
2.5	—	1.861	0	0.244	0	11.127	0
3.0	—	2.354	0	0.243	0	10.629	0
0.0	22.0	0.195	0.019	0.252	0.017	17.653	0.082
1.0	22.4	0.628	0.059	0.251	0.031	15.846	0.064
2.0	15.8	1.476	0.045	0.245	0.016	13.868	0.018
3.0	—	2.513	0	0.240	0	12.411	0
$W_E < 0$	23.2	1.187	0.148	0.261	0.088	8.750	0.156
$W_E > 0$	—	0.392	0	0.268	0	7.334	0
$\underline{W_E = 0}$	23.5	0.253	0.058	−0.260	0.038	11.330	0.123
$\underline{W_E < 0}$	35 + 55	0.902	0.162	−0.262	0.028	7.081	0.068
$\underline{W_E > 0}$	—	0.564	0	−0.271	0	8.895	0

wind forcing in the upper layers helps generate large baroclinic instability growth rate, even slightly larger than for the purely thermally driven case, even in the cases where no oscillations are present. Of course there are several limitations to the relevance of these calculations: we do not consider the intrinsic limitations of the QG framework (the slope of the isopycnals for instance), we assume the linear growth rate to be relevant to the nonlinear evolution of the anomalies, we do not consider the spatial structure of the mean stratification and circulation in these local calculations. Furthermore, we perform the calculation on the time-averaged temperature fields whose available potential energy has already been released by baroclinic instability, and finally we do not take into account the dissipation of PV anomalies through thermal damping, mainly by horizontal diffusion (the major sink of temperature variance), such that the most unstable wave might not be the right one if its wavelength is too short. Nevertheless, it appears that an explanation for the damping effects of winds solely in terms of baroclinic instability is inadequate.

There may be some rationale for a direct damping of temperature anomalies by upward Ekman pumping. Assuming the wind forcing acts only through the Ekman pumping W_E at the base of the mixed layer, the additional term for the total derivatives of the temperature fluctuations is like

$$\partial T'/\partial t = -W_E \partial T'/\partial z. \tag{14}$$

Assuming an exponential profile of the temperature anomalies with depth: $T' \propto \exp(kz)$, with k of the order of (500 m)$^{-1}$, the temperature anomaly fluctuation evolves with time due to the Ekman pumping as $T' \propto \exp(-W_E k t)$. If $W_E > 0$, the anomalies are damped with an e-folding timescale $\tau = (W_E k)^{-1} = O(\text{yr})$ for $W_E = 3 \times 10^{-6}$ m s^{-1}; conversely, the anomalies are enhanced for downward Ekman pumping. Note that this is the order of magnitude of the growth rate of the long-wave baroclinic instability. This argument is rather heuristic, but is consistent with the numerical experiments. As the variability (and its source of energy) is concentrated in the northern part of the domain, the increase in wind forcing reinforces the upward Ekman pumping in the northern third of the domain, which acts as a damping term.

To test this hypothesis further, we use different profiles for the wind stress such that the implied Ekman pumping is now constant, negative in one case (''subtropical gyre''), positive in the other (''subpolar gyre''). The former wind stress reinforces the thermally driven circulation in the thermocline through an anticyclonic gyre, while the latter induces a barotropic cyclonic gyre that is opposed to the upper thermohaline cell. The results support our hypothesis: while the negative Ekman pumping increases the variability as compared to the solely thermally driven case, the upward pumping totally annihilates the variability. Once again, it is difficult to sort out the influence of the wind forcing on the variability through the damping of anomalies, because of its large influence on the mean circulation. As an attempt to justify the major role of the damping as discussed above, we reproduce the experiments with an opposite surface heat flux. The damping role of positive Ekman pumping now coincides with a reinforcement of the thermohaline cell while the destabilizing role of negative Ekman pumping corresponds to a weakened overturning. For a heat flux varying linearly from −45°W m^{-2} at 20°N to 45°W m^{-2} at 60°N, oscillations are sus-

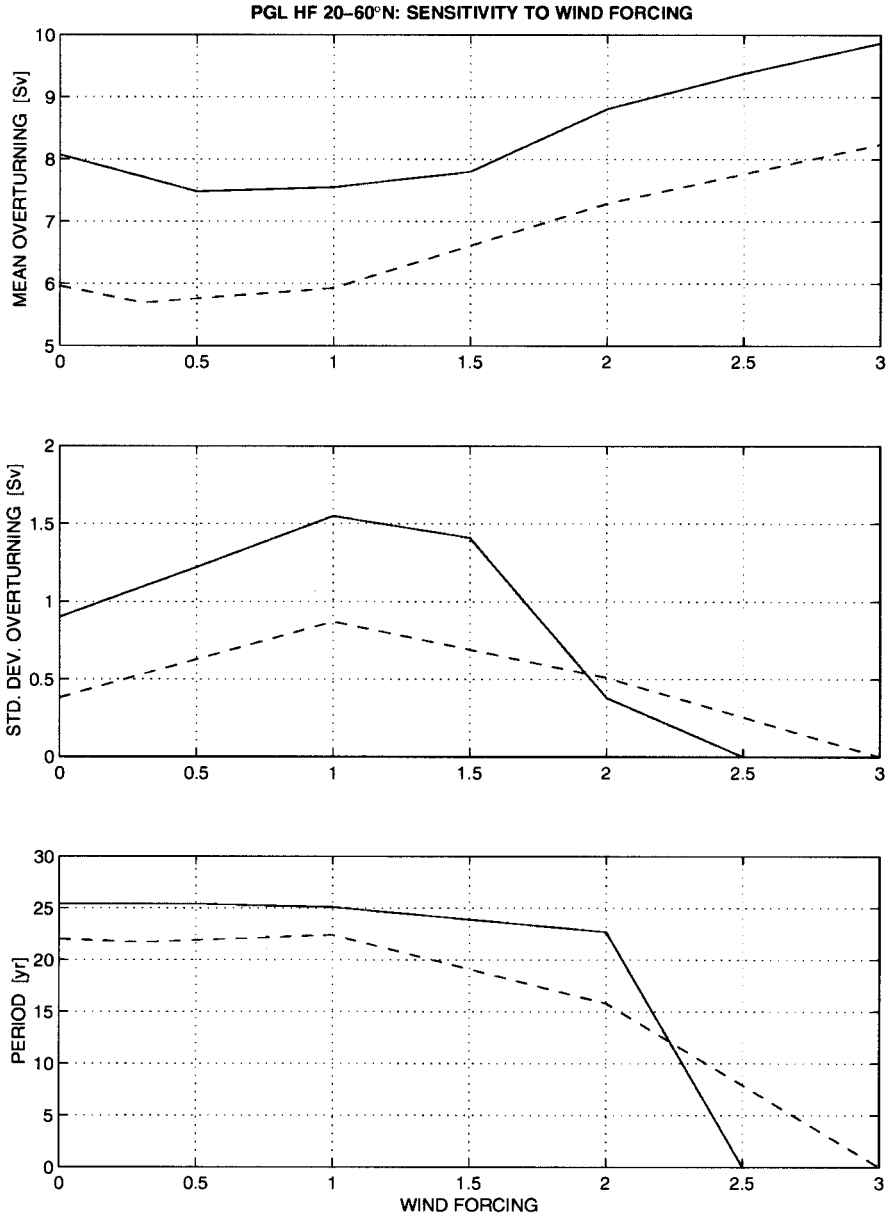

FIG. 12. Sensitivity to wind forcing in the L160 coarse-resolution simulation. (a) Mean and (b) standard deviation of the maximum overturning streamfunction, and (c) oscillation period as a function of the factor multiplying the analytical wind stress of Bryan (1987), for vertical tracer diffusivities of 10^{-4} (solid line) and 0.5×10^{-4} m^2 s^{-1} (dashed line).

tained with time-averaged overturning of 23 Sv but an irregular period O(23 yr). When a zonal wind stress decreasing linearly from 0.3 kg m^{-1} s^{-2} at 20°N to -0.3 kg m^{-1} s^{-2} at 60°N is added, which drives an upward Ekman pumping of 1.5×10^{-6} m s^{-1}, the oscillations disappear although the maximum overturning is now increased to 49 Sv. If the opposite wind stress is imposed at the surface, the oscillations are *enhanced.* They are still irregular, with main periods of 35 and 55 yr, although the mean overturning is reduced to 16 Sv. Clearly, it is the *upward* Ekman pumping that plays a role in damping the interdecadal thermohaline variability.

6. Interaction with the bottom topography

The damping effect of topography on the baroclinic modes have been stressed by various authors (Greatbatch et al. 1997; Winton 1997). Although the surface intensification of the variability suggests that the effect of bottom topography is rather remote, we briefly il-

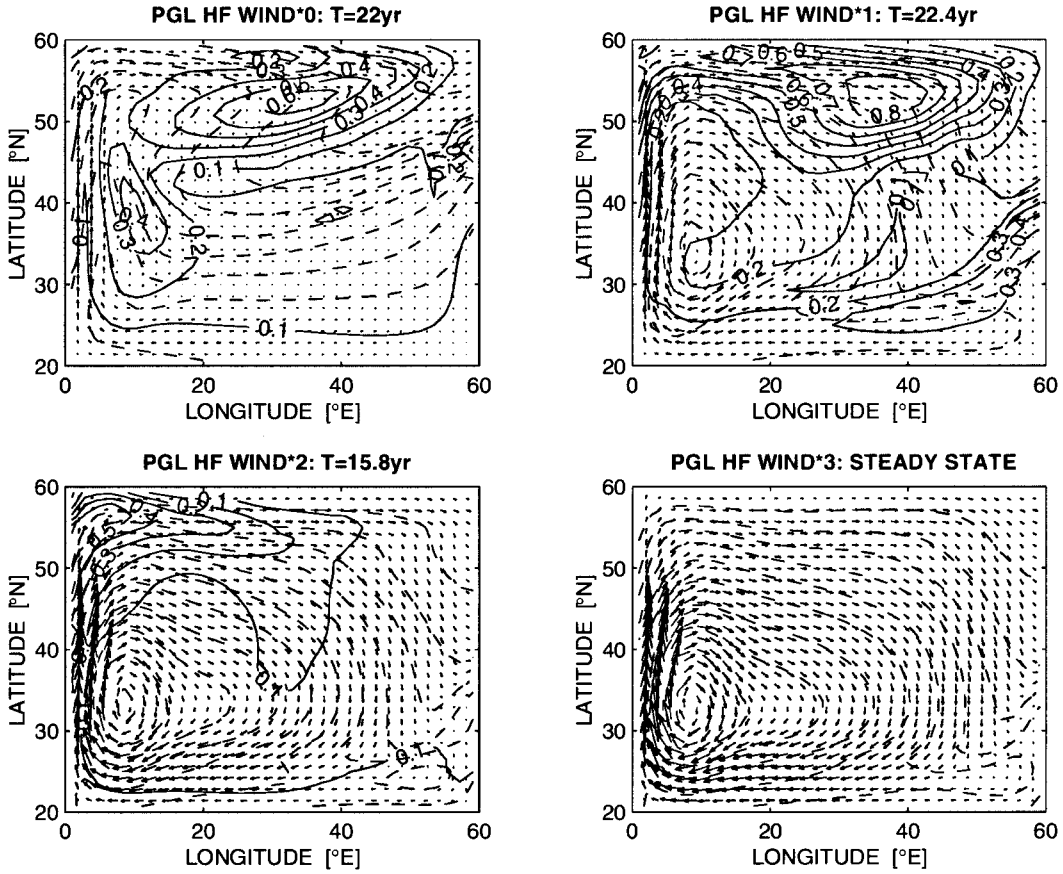

FIG. 13. Comparison of the variability for different wind forcing amplitude, for experiment L160 with 0.5×10^{-4} $m^2\ s^{-1}$ vertical diffusivity. Temperature in the upper 250 m: standard deviation (solid contours with labels every 0.1°C) and time-averaged temperature (dashed contours every 2°C). Time averaged velocities in the upper 250 m (0.2 cm s^{-1} per degree of latitude or longitude).

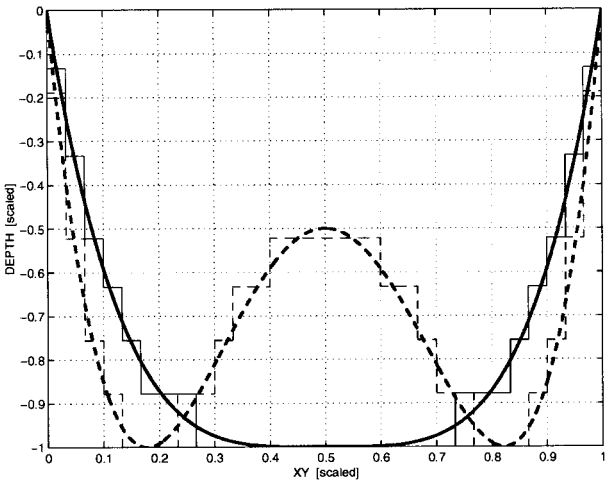

FIG. 14. Analytical topography profiles used in MOM experiments and their discretization on 30 horizontal grid points and the 15 vertical levels: f1 (solid), f2 (dashed).

lustrate hereafter this sensitivity by implementing various bottom topography as functions of latitude and longitude (Fig. 14) within MOM in the basic configuration that was studied extensively in sections 2 and 3 (experiment L160). Table 4 summarizes the results.

The first experiment implements gently sloping coastal boundaries instead of vertical walls. While such a bowl-shaped topography has a damping effect on the variability as compared to the flat-bottom case (the amplitude of the oscillations is reduced by a factor of 5, both in kinetic energy and mean surface temperature), the oscillations remain regular with a period shortened to 16 yr.

The second experiment adds a large mid-Atlantic ridge in the center on the basin on top of the previous sloping boundaries. For the standard parameters, the model settles down in a steady state. However, if the horizontal tracer diffusivity is reduced to 500 $m^2\ s^{-1}$, the oscillations are sustained again with a significant amplitude: temperature anomalies in the upper 250 m reach 5°C (not shown). More surprising is that a further decrease in the horizontal diffusivity (350 $m^2\ s^{-1}$) re-

TABLE 4. Sensitivity of the oscillations to bottom topography. Experiments are based on the MOM1 L160 experiment of section 3 to which bottom topography has been added as analytical function of x and y: f1 is a simple bowl function, while f2 has an additional bump in the center of the domain mimicking a mid-Atlantic ridge (see Fig. 14). $H = 4500$ m: x and y are nondimensional scaling of longitude and latitude varying between 0 and 1. The default horizontal diffusivity K_H is 700 $m^2\ s^{-1}$, unless stated otherwise. KE density: total kinetic energy density, mean and standard deviation (0.1 kg $m^{-1}\ s^{-2}$). PHT: maximum advective poleward heat transport, mean, and standard deviation (PW). SST: mean ocean surface temperature (0–50 m), mean and standard deviation (°C). Tbot: time-averaged mean bottom temperature (3950–4500 m) (°C).

Experiment: bottom depth, K_H/($m^2\ s^{-1}$)	Oscillation period (year)	KE density		PHT		SST		Tbot
		Mean (0.1SI)	Stdev (0.1SI)	Mean (PW)	Stdev (PW)	Mean (°C)	Stdev (°C)	Mean (°C)
H	26.0	0.262	0.045	0.2540	0.0250	13.643	0.095	3.187
$H \times$ f1(x) $\times$ f1(y)	16.0	0.345	0.006	0.2610	0.0058	12.683	0.018	3.141
$H \times$ f2(x) $\times$ f1(y)	0.0	0.360	0	0.2606	0	12.823	0	3.049
-, $K_H = 500$	21.2	0.399	0.182	0.2959	0.1164	13.224	0.319	2.947
-, $K_H = 350$	~29.1	0.427	0.118	0.2730	0.0595	13.184	0.202	2.995
$H \times$ f1(x) $\times$ f2(y)	18.8	0.378	0.037	0.2618	0.0207	12.903	0.057	3.073
$-H \times$ f1(y)	32.4	0.593	0.104	0.2535	0.0303	12.766	0.151	2.792
$-H \times$ f1(x)	28.3	0.302	0.027	0.2684	0.0387	13.20	0.068	3.179

duces the amplitude of the oscillations, as the variability loses its regularity.

Finally, let us rotate the model mid-Atlantic ridge by 90° so that it is zonal, and also restore horizontal diffusivity to its default value, 700 $m^2\ s^{-1}$. This specific and highly imaginary topography induces only a slight decrease (20%) in the amplitude of the oscillations, but a larger reduction in the period (18.8 yr instead of 26), compared with the flat-bottom experiment.

Ubiquitous about these oscillations is the intricate interplay of geometry, forcing, and parameters that gives rise to sustained or damped oscillations. The damping influence of bottom topography is not more radical than the other damping factors but certainly more difficult to assess (in terms of an e-folding timescale, for instance), since the influence of the bottom slope on baroclinic instability and planetary waves is not trivial (also the models' representation of topography might be an issue). As for other damping factors, the central question is whether the mean circulation is not as favorable to long-wave baroclinic instability (i.e., the source term of the variability through the growth rate of baroclinic instability is weaker), or the damping of anomalies is stronger. The latter role is emphasized by Greatbatch et al. (1997) through the bottom pressure torque on baroclinic waves. Given the scale of the topographic features, which is close to the horizontal wavelength of the interdecadal modes, a quasigeostrophic analysis is necessarily limited, but no other tool is yet available to us for estimating the growth rate of baroclinic instability in the presence of bottom slope. We shall then leave the stability analysis of these simulations unsettled for now until the appropriate tools are adapted for such a task.

However, such a sensitivity of the oscillation period and amplitude to details of the bottom topography or the subgridscale parameterization does not encourage one to make any prediction on the relevance of such thermohaline modes to explain the decadal or interdecadal variability observed in the North Atlantic.

7. Discussion and conclusions

We have addressed two related classes of problems in this paper. One is related to the basic mechanism of interdecadal oscillations in the thermohaline circulation, and the factors producing their period. The second is related to how sensitive these oscillations are to the ''complicating'' factors of mesoscale eddies, coupling with the atmosphere, wind forcing, and topography.

From an elementary scaling perspective, the oscillation period varies as a function of the model parameters in reasonable agreement with the zonal extent of the basin divided by the mean geostrophic current. The latter scales also as the speed of baroclinic Rossby waves based on the potential vorticity gradient given by the mean stratification (rather than the planetary β effect).

In the non-eddy-resolving experiments the baroclinic instability acts at large scales and is rather weak. In higher resolution, less viscous experiments, by contrast, baroclinic instability can produce a vigorous field of mesoscale eddies. Nevertheless, over a reasonably broad parameter regime interdecadal variability retains a dominant period around 30 yr, and with a similar amplitude. The turbulent (eddy) kinetic energy varies also largely on these timescales. The regularity of the oscillations decreases with higher resolution, as might be expected, as shorter (annual to interannual) and longer (roughly twice the main period) timescale emerge.

The potential effects of interactions with the atmosphere were investigated by coupling the ocean model to an atmospheric energy balance model including more processes than previous studies. The oscillations showed little sensitivity to the exchange coefficient for (possibly unrealistic) high vertical diffusion, whereas for low diffusion a critical range for the coupling coefficient (of the order of 10 to 20 W $m^{-2}\ K^{-1}$) was found, on either side of which oscillations slowly die out. However, for a larger and more realistic meridional temperature con-

trast, the oscillations were no longer sensitive to the exchange coefficient. Note, too, that in the steady regime the oscillations are damped on a very long timescale ($\gg 10^2$ yr) so that the addition of a varying forcing (representing the weather, say) could likely act to sustain the oscillations (see also Griffies and Tziperman 1995; Delworth and Greatbatch 2000). Oceanic mesoscale turbulence might also play a similar role, the highly nonlinear mesoscale eddies effectively acting as a stochastic forcing on the thermohaline circulation.

When wind forcing was included, and with a (realistically) small vertical mixing of heat, the oscillations were sustained for approximately realistic levels of wind, being damped only at wind levels well above the climatological forcing. Interestingly, these steady states are still (by linear analysis) susceptible to long-wave instability, because of the large shear induced by the windstress in the surface layers. However, a damping of surface intensified temperature anomalies through upward Ekman pumping seems to give approximately the correct *e*-folding timescale, and to agree with the model simulations.

Finally, we find that topography generally has a damping role, in agreement with various other previous work. The damping seems to be sensitive to the orientation of the main topographic features and the mean circulation or adjustment waves propagation. The mid-Atlantic ridge would be expected to have a damping role, and it remains to be seen how the resolution of the eddies would interact with the bottom topography to excite or damp the interdecadal mode.

The broad messages emerging from this study are thus as follows. Interdecadal oscillations of the thermohaline circulation are relatively insensitive to various changes in model resolution, and corresponding changes in horizontal diffusion coefficients, although the oscillations are much less regular as the resolution increases and mesoscale eddies are generated. Typically, the oscillations weaken as the vertical diffusivity coefficient falls. The oscillations are retained when the model is coupled to a simple atmospheric energy-balance model, although the oscillations may be damped if the effective exchange coefficient with the atmosphere is either sufficiently small or sufficiently large. The addition of wind forcing generally weakens the oscillations, possibly killing them altogether. Finally, topography has a generally damping effect, although the orientation of the topography was found to be important. Overall, our results would suggest that the real ocean (aside from the effects of mesoscale eddies) might not be in a parameter regime that supports self-sustained interdecadal oscillations under constant forcing, because of the cumulative damping of small vertical mixing, wind forcing, and bottom topography. On the other hand, the damping rates appear small, and thus stochastic forcing, from either atmospheric or oceanic transients (baroclinic eddies in either case) may well act to sustain the oscillations. If so, this would suggest that the parameter regime for interdecadal oscillations in an eddy-resolving ocean model (and indeed the ocean itself) would be larger than for a non-eddy-resolving model. Given the expense that investigating this would entail (integrating a mesoscale-eddy-resolving ocean model in a realistic domain for hundreds of years) it remains a task for the future. Further, it would suggest that an ocean model coupled to an atmospheric GCM, or any variable atmospheric model, would be more likely to produce interdecadal oscillations, although the oscillations need not be in any nontrivial sense a ''coupled mode.'' Although the presence of the oscillations is, overall, a relatively robust feature when some kind of stochastic forcing is present, the behavior is sufficiently complex and sufficiently parameter sensitive that an unambiguous association of a particular set of parameters or a particular class of behavior with the real ocean is not currently possible.

Acknowledgments. This work has been supported by the NSF Grant ATM 9710285. We wish to thank T. Delworth, S. Griffies, and M. Winton at GFDL; two anonymous reviewers for valuable comments on the original manuscript; and A. M. Treguier and L. Dubus at Laboratoire de Physique des Océans for providing the initial Matlab version of the QG baroclinic instability routines.

REFERENCES

Beckmann, A., 1988: Vertical structure of midlatitude mesoscale instabilities. *J. Phys. Oceanogr.,* **18,** 1354–1371.

Bjerknes, J., 1964: Atlantic air–sea interactions. Advances in Geophysics, Vol. 10, Academic Press, 1–82.

Bryan, F. O., 1987: Parameter sensitivity of primitive equation ocean general circulation models. *J. Phys. Oceanogr.,* **17,** 970–985.

Bryan, K., 1991: Poleward heat transport in the ocean: A review of a hierarchy of models of increasing resolution. *Tellus,* **43,** 104–115.

Chen, F., and M. Ghil, 1995: Interdecadal variability of the thermohaline circulation and high-latitude surface fluxes. *J. Phys. Oceanogr.,* **25,** 2547–2568.

——, and M. Ghil, 1996: Interdecadal variability in a hybrid coupled ocean–atmosphere model. *J. Phys. Oceanogr.,* **26,** 1561–1578.

Chu, P. C., Y. Chen, and S. Lu, 1998: On Haney-type surface thermal boundary conditions for ocean circulation models. *J. Phys. Oceanogr.,* **28,** 890–901.

Chylek, P., and J. A. Coakley, 1975: Analytical analysis of a Budyko-type climate model. *J. Atmos. Sci.,* **32,** 675–679.

Colin de Verdière, A., 1986: On mean flow instabilities within planetary geostrophic equations. *J. Phys. Oceanogr.,* **16,** 1981–1984.

——, and T. Huck, 1999: Baroclinic instability: An oceanic wavemaker for interdecadal variability. *J. Phys. Oceanogr.,* **29,** 893–910.

——, and T. Huck, 2000: A 2 degree of freedom dynamical system for interdecadal oscillations of the ocean–atmosphere. *J. Climate,* **13,** 2801–2817.

Delworth, T., S. Manabe, and R. J. Stouffer, 1993: Interdecadal variations of the thermohaline circulation in a coupled ocean–atmosphere model. *J. Climate,* **6,** 1993–2011.

——, and R. J. Greatbatch, 2000: Multidecadal thermohaline circulation variability excited by stochastic surface flux forcing. *J. Climate,* **13,** 1481–1495.

——, and M. E. Mann, 2000: Observed and simulated multidecadal variability in the North Atlantic. *Climate Dyn.,* **16,** 661–676.

Fanning, A. F., and A. J. Weaver, 1996: An atmospheric energy-moisture balance model: climatology, interpentadal climate change, and coupling to an OGCM. *J. Geophys. Res.,* **101,** 111–128.

——, and ——, 1998: Thermohaline variability: The effects of horizontal resolution and diffusion. *J. Climate,* **11,** 709–715.

Gill, A. E., J. S. A. Green, and A. J. Simmons, 1974: Energy partition in the large-scale ocean circulation and the production of mid-ocean eddies. *Deep-Sea Res.,* **21,** 499–528.

Graves, C. E., W.-H. Lee, and G. R. North, 1993: New parameterizations and sensitivites for simple climate models. *J. Geophys. Res.,* **98,** 5025–5036.

Greatbatch, R. J., and S. Zhang, 1995: An interdecadal oscillation in an idealized ocean basin forced by constant heat flux. *J. Climate,* **8,** 81–91.

——, and K. A. Peterson, 1996: Interdecadal variability and oceanic thermohaline adjustment. *J. Geophys. Res.,* **101,** 20 467–20 482.

——, ——, and H. Roth, 1997: Interdecadal variability in a coarse resolution model with North Atlantic bottom topography. Technical Report, Department of Oceanography, Dalhousie University, Halifax, Nova Scotia, Canada.

Griffies, S. M., and E. Tziperman, 1995: A linear thermohaline oscillator driven by stochastic atmospheric forcing. *J. Climate,* **8,** 2440–2453.

Huang, R. X., and R. L. Chou, 1994: Parameter sensitivity of the saline circulation. *Climate Dyn.,* **9,** 391–409.

Huck, T., A. Colin de Verdière, and A. J. Weaver, 1999a: Interdecadal variability of the thermohaline circulation in box-ocean models forced by fixed surface fluxes. *J. Phys. Oceanogr.,* **29,** 865–892.

——, A. J. Weaver, and A. Colin de Verdière, 1999b: On the influence of the parameterization of lateral boundary layers on the thermohaline circulation in coarse-resolution ocean models. *J. Mar. Res.,* **57,** 387–426.

Killworth, P., 1985: A two-level wind and buoyancy driven thermocline model. *J. Phys. Oceanogr.,* **15,** 1414–1432.

Kushnir, Y., 1994: Interdecadal variations in North Atlantic Sea Surface Temperature and associated atmospheric conditions. *J. Climate,* **7,** 141–157.

Ledwell, J. R., A. J. Watson, and C. S. Law, 1993: Evidence for slow mixing across the pycnocline from an open-ocean tracer-release experiment. *Nature,* **364,** 701–703.

Mann, M. E., R. S. Bradley, and M. K. Hughes, 1998: Global-scale temperature patterns and climate forcing over the past six centuries. *Nature,* **392,** 779–787.

McCartney, M. S., R. G. Curry, and H. F. Bezdek, 1996: North Atlantic's transformation pipeline chills and redistributes subtropical water. *Oceanus,* **39,** 19–23.

Pacanowski, R., K. Dixon, and A. Rosati, 1991: The GFDL Modular Ocean Model, Users Guide Version 1.0. GFDL Ocean Group Tech. Rep. 2, 46 pp.

Pedlosky, J., 1979: *Geophysical Fluid Dynamics.* Springer-Verlag, 624 pp.

Samelson, R. M., and G. K. Vallis, 1997: Large-scale circulation with small diapycnal diffusion: The two-thermocline limit. *J. Mar. Res.,* **55,** 223–275.

Seager, R., Y. Kushnir, and M. A. Cane, 1995: On heat flux boundary condition for ocean models. *J. Phys. Oceanogr.,* **25,** 3219–3230.

Stammer, D., and C. W. Böning, 1992: Mesoscale variability in the Atlantic ocean from Geosat altimetry and WOCE high-resolution numerical modeling. *J. Phys. Oceanogr.,* **22,** 732–752.

Timmermann, A., M. Latif, R. Voss, and A. Grotzner, 1998: Northern hemispheric interdecadal variability: A coupled air–sea mode. *J. Climate,* **11,** 1906–1931.

Vallis, G. K., 2000: Large-scale circulation and production of stratification: Effects of wind, geometry, and diffusion. *J. Phys. Oceanogr.,* **30,** 933–954.

Winton, M., 1996: The role of horizontal boundaries in parameter sensitivity and decadal-scale variability of coarse-resolution ocean general circulation models. *J. Phys. Oceanogr.,* **26,** 289–304.

——, 1997: The damping effect of bottom topography on internal decadal-scale oscillations of the thermohaline circulation. *J. Phys. Oceanogr.,* **27,** 203–208.